TÉCNICO LISBOA

Topology optimization for elastic buckling of structures at macro- and micro-scales

Mariana João de Almeida Figueiredo

Thesis to obtain the Master of Science Degree in

Aerospace Engineering

Supervisor: Prof. Miguel António Lopes de Matos Neves

Examination Committee

Chairperson: Prof. Filipe Szolnoky Ramos Pinto Cunha
Supervisor: Prof. Miguel António Lopes de Matos Neves
Member of the Committee: Prof. Pedro Samuel Gonçalves Coelho

January 2021

To my dear friends

Declaration:

I declare that this document is an original work of my own authorship and that it fulfills all the requirements of the Code of Conduct and Good Practices of the Universidade de Lisboa.

Acknowledgments

Firstly, I would like to thank to my supervisor, Prof. Miguel Matos Neves, for the guidance, motivation, transmission of knowledge and useful discussions.

Secondly, I would like to thank Prof. Krister Svanberg for kindly providing his Matlab version of the Method of Moving Asymptotes.

Declaração:

Declaro que o presente documento é um trabalho original da minha autoria e que cumpre todos os requisitos do Código de Conduta e Boas Práticas da Universidade de Lisboa.

Resumo

Este trabalho foca-se no problema de estabilidade de estruturas construídas a partir de materiais celulares periódicos e no problema de obtenção de estruturas ótimas para maximização da carga crítica.

O problema de estabilidade é abordado em escalas micro, macro e mistas através de uma teoria de estabilidade linear. No problema à macroescala, as propriedades efetivas são obtidas a partir da teoria da homogeneização. Para resolver o problema considerando o acoplamento macro-micro, a metodologia proposta aplica a mesma discretização de elementos finitos para ambos os domínios, com o objetivo de implementar e verificar a equação de acoplamento das duas escalas.

A solução para a maximização da carga crítica de estruturas é obtida pela otimização da topologia com uma abordagem baseada na densidade material, onde se optou não incluir o caso de não diferenciabilidade da carga critica quando existem cargas de instabilidade repetidas. O esquema utilizado para a atualização das variáveis de projeto é o Método das Assíntotas Móveis.

As implementações desenvolvidas foram aplicadas a casos tipos e os resultados comparados com exemplos similares encontrados na literatura. A implementação do problema de estabilidade com acoplamento macro-micro permitiu testar a aplicação da equação de acoplamento. Os resultados obtidos foram analisados em relação aos valores limite (macro e micro). Tanto quanto é conhecimento da autora, não existem na literatura resultados semelhantes.

Palavras-chave: Estabilidade, Materiais Celulares, Homogeneização, Estabilidade Multi-escala, Otimização de Topologia, Elementos Finitos

Declaration:

I declare that this document is an original work of my own authorship and that it fulfills all the requirements of the Code of Conduct and Good Practices of the Universidade de Lisboa.

Abstract

This work focuses on the stability problem of structures built from periodic cellular materials and on the problem of obtaining optimal structures with maximized buckling strength.

The stability problem is addressed at micro-, macro- and mixed-scales by means of a linearized buckling theory. When considering the macro-scale problem, the effective properties are obtained from the homogenization theory. To solve the problem of macro-scale and micro-scale coupling, the proposed methodology is obtained by applying the same finite element discretization to macro-scale and micro-scale domains in order to implement and verify the coupling equation of the two scales.

The solution for maximum buckling strength of structures is obtained by topology optimization with a material density based approach, where it was decided not to include the case of non-differentiability of the critical load when repeated buckling loads exist. The used design variables updating scheme is the Method of Moving Asymptotes.

The computational implementations are applied to benchmark examples and the results are compared with similar ones found in the literature. The implementation of the macro- and micro- coupled instability problem enables the application of the coupled instability equation. Similar results, as far as the author knows, do not exist in the literature.

Keywords: Stability, Cellular Materials, Homogenization, Multi-scale Buckling, Topology Optimization, Finite Elements

Contents

List of Tables

List of Figures

Nomenclature

Greek symbols

α	Displacement parameter.
Γ	System's boundary.
δ	Variation.
ε	Unit cell's scale parameter.
$\tilde{\boldsymbol{\varepsilon}}$	Macroscopic strain field.
λ	Load factor.
ν	Poisson's ratio.
Π	Total potential energy.
$\boldsymbol{\sigma}$	Stress tensor.
$\boldsymbol{\sigma^0}$	Stress tensor at the micro-scale level, resulting from a macroscopic strain field.
ϕ	Instability mode field.
χ	Characteristic displacement.
ψ	Virtual instability mode field.
Ω	System's domain.

Roman symbols

A	Total elastic strain energy.
$\boldsymbol{B}$	Strain-displacement matrix.
c	Compliance.
$\boldsymbol{e}$	Strain tensor.
E	Young's modulus.
$\boldsymbol{E}$	Constitutive matrix.

f Body force.

f' Maximum allowed total volume fraction.

$\boldsymbol{F}$ Load vector.

g Constraint function.

$\boldsymbol{G}$ Geometric stiffness matrix.

H Weight factor.

$\boldsymbol{I}$ Identity matrix.

$\boldsymbol{J}$ Jacobian matrix.

$\boldsymbol{K}$ Stiffness matrix.

N Shape function.

p Penalization factor.

r_{min} Filter radius.

R Potential of applied forces.

t Surface traction.

u Displacement field.

v Virtual displacement field.

$\boldsymbol{V}$ Nodal adjoint displacement field.

$\boldsymbol{x}$ Macro-scale spatial variables.

$\mathbf{x}$ Design variables.

$\boldsymbol{y}$ Micro-scale spatial variables.

Y Unit cell's domain.

Subscripts

cr Critical condition.

i, j, k, m, p, q, r, s Computational indexes.

x Macro-scale dependence.

xy Macro-scale and micro-scale dependence.

y Micro-scale dependence.

Superscripts

ε	Dependence on the unit cell's scale parameter.
H	Homogenized quantity.
h	Interpolated quantity.
ref	Reference condition.
T	Transpose.

List of Acronyms

MMA Method of Moving Asymptotes.

RVE Representative Volume Element.

SIMP Solid Isotropic Material with Penalization.

Chapter 1

Introduction

1.1 Motivation

Buckling occurs when a structure is subjected to an increasing load that, after reaching some critical value, results in a sudden change of its equilibrium configuration. In the case of gradually increased load, this static equilibrium position modification (which can be described as a sideways deflection) causes the vanishing of the structure's stiffness and may occur before the structure starts to yield or fails. This means that when a component of a given assembly buckles, the remaining ones need to support the load beyond this critical value (the one that caused the buckling).

This makes the buckling phenomena an important factor when assessing the design of a structure. Particularly in the aerospace sector, since weight plays a crucial role, lightweight structures are widely used and their inherent slenderness makes stability one of the key requirements when designing aerospace structures.

Lightweight structures are typically built from low density cellular materials, which have found a wide range of applicability, including, for instance, infill structures for additive manufacturing. However, the strength capacity of these materials is also limited by micro-structural instabilities which may occur when their slender structural members are subjected to compressing loads [1].

This means that structures built with periodic cellular materials can buckle on multi spacial scale levels (macro-scale, micro-scale and mixed-scale levels).

There is, therefore, the need to design structures as well as materials for improved buckling performance. One of the most attractive ways of finding optimal designs for a given set of constraints on it is topology optimization, since it doesn't rely on any preconceived shape of the structure. In fact, topology optimization "has been recognized as one of the most effective approaches at the conceptual design phase of most engineering applications" [2].

In the aerospace field, one of the first studies regarding this method was the optimal design of the internal structure of a wing for a supersonic aircraft, where the purpose was to determine the arrangement of ribs and spars that minimizes the structure's compliance (deformation) [3]. Following that, the method has been applied to other aerostructures optimization for minimum compliance such as a fuse-

lage structure [4], a wing with an outboard X-stabilizer [5] and non-conventional aircraft configurations, namely a Blended-Wing-Body commercial passenger aircraft and an Unmanned Air Vehicle structure [6].

Moreover, the use of topology optimization combined with other techniques has also drawn some attention. For instance, Oktay et al. [7] presented a methodology for the parallel use of topology optimization for compliance minimization and Computational Fluid Dynamics and applied it to a wing's cross-section. Another example is the framework presented in [8], where a wing is optimized for minimum lift-induced drag using simultaneously structural topology optimization and aerodynamic shape optimization.

However, in the aerospace industry, the number of real-world design problems where topology optimization was applied is still not very significant [9]. These include, for instance, the redesign of the wing box ribs for weight reduction of the A380 using topology optimization techniques [10].

Regarding structural topology optimization where buckling is considered, fewer studies have been found, even though stability problems have been addressed since the early times of structural optimization [11].

In the context of buckling strength of periodic materials, Neves et al. [12] proposed a methodology for the maximization of the critical load for micro-structures exhibiting micro-scale buckling modes with the same periodicity of the cellular material. Later, this work was extend to include buckling modes of different wave-lengths by means of the Bloch-wave theory [13] and recently a further extension, which includes the complete Bloch wave analysis, is provided in [1].

As for the macro-scale buckling strength of structures based on continuum models, optimality conditions for single and multiple eigenvalues are presented in [14] and a methodology for the maximization of the linearized buckling load using topology optimization is presented in [15]. A recent review on the topic of topology optimization addressing buckling can be found in [11].

Regarding the problem of obtaining optimal aerostructures using topology optimization including linearized buckling behaviour, only a recent study was found, where topology optimization techniques with buckling constraints are applied to the Common Research Wing Model for the optimization of the skin of the wing box [2].

By these considerations, it can be understood that the application of topology optimization in the industrial environment is still quite an open topic and that that is even more evident when addressing the stability of structures. Furthermore, while computational models as well as studies have been developed for the calculation and optimization of linearized buckling loads at macro- and micro-scale levels (even though not very extensively), no such implementations were found for the mixed-scale buckling case.

1.2 Topic and Methods Overview

Buckling is essentially a non-linear phenomenon. However, in this work, only linearized theories are used to describe it. This is done, since full non-linear analysis are more computationally demanding and linearized theories can predict buckling behaviour correctly in the considered cases, where before

instability occurs the structural response is linear elastic.

Here, the instability phenomena of structures built from solids with periodic micro-structures is addressed by means of a linearized elasticity theory based on a double-scale asymptotic technique [16]. In [16], equations describing buckling at macro-scale and micro-scale levels and a new equation regarding mixed-scale buckling behaviour are obtained.

When considering the macro-scale level buckling behaviour, one needs information on the material constants. Since for this type of solids, the material properties are not constant throughout the entire domain and because they are built as a periodic repetition of a micro-structure, the averaged/effective material properties can be calculated by considering one of these cells. These are referred to as RVE based methods. Here, and as also obtained in [16], the homogenization theory, which is a result of the application of asymptotic techniques, is used to obtain such properties.

There exist in the literature other methods for calculating such constants, namely standard mechanics procedures. Comparison between some of these methods is presented in [17], where both the homogenization and standard mechanics RVE based approaches are addressed, concluding that "homogenization theory is preferable over standard mechanics of materials approaches for periodic composites even when the material is only locally periodic".

Concerning the micro-scale buckling behaviour, the implementation here given is limited to instability modes having the same periodicity of the unit cell, which is known not to be the only scenario. However, and although out of scope of this work, the implemented theory can be generalized for non-periodic conditions by means of the Floquet-Bloch wave theory, as done in [1].

Implementations and methods to address the coupled instability problem based on the equation provided in the used bifurcation theory from [16] were not found. However, and although not used in this dissertation, scale-coupling methods in solid mechanics are available, such as the Schwarz alternating method, developed for the multiscale coupling in the finite deformation range [18].

In this work, as already mentioned, optimal structures are obtained by means of topology optimization. The general idea of the method is to find black-and-white designs (solid-and-void designs) where no preconceived shape was assigned to the considered structure. Its classic formulation, also known as *binary problem*, is ill-posed, as a series of feasible and non-convergent designs can be obtained [19].

One of the ways of overcoming this problem is the use of the aforementioned homogenization method, which enables the inclusion of intermediate material density values in the formulation. Many authors have used it in the context of topology optimization (see, for instance [20], [21] and [22]). However, this approach poses some drawbacks, including the sometimes difficult manufacturability of the final structure and the fact that the optimal micro-structure is not always known [19].

In this dissertation and as commonly done in topology optimization, a *density-based approach* is used to relax the binary problem, since it doesn't present the difficulties from the homogenization method and requires less effort in its implementation.

To solve the optimization problem, several sequential explicit, convex approximation techniques are available, such as Sequential Linear Programming, Sequential Quadratic Programing, Convex Linearization and the Method of Moving Asymptotes (MMA) [23]. In this work, and since it has proven to be the

one that provides converged solutions for a wider range of problems, the MMA is used.

When considering buckling in the optimization process, some difficulties arise, namely the appearance of artificial buckling modes present in low density regions and repeated buckling loads, which may lead to numerical instabilities.

To overcome the issue of buckling modes in low density regions, Neves et al. [15] suggested that, when assembling the geometric stiffness matrix, the elemental matrices corresponding to elements with densities smaller than a predefined value should be assigned a null stress value, which corresponds to being ignored in the calculations. This method, however, causes oscillations in the solution, since abrupt changes in the objective function and sensitivities occur [24]. The method proposed in [24], which is based on different interpolations of the Young's modulus for the stiffness and geometric stiffness matrices, is here followed. This method has been used in some works (for instance in [25], where a large-scale topology optimization approach with linearized buckling criteria is presented) and proven to be efficient in mitigating this problem.

Although out of scope of this work, solutions on overcoming the problem of non-diferentiability of the objective function in the case of repeated buckling loads can be found in [25] or [26].

1.3 Objectives

This dissertation aims, then, to answer to the question of how to calculate and implement the buckling response of a structure built from solids with periodic micro-structure based on a linearized stability theory. This includes a review of the existing methods for addressing buckling at separated macro- and micro-scales as well as the study of the mixed-scale problem with the objective of providing a computational implementation capable of calculating coupled instability loads and modes.

Furthermore, this work seeks to provide a simple numerical implementation for the maximization of the macro-scale critical buckling load of structures. For that purpose, a review of existing implementations for the compliance minimization of structures (including the use of existing commercial codes) is here done, which is further extended to address linearized buckling behavior in the optimization process.

The main objective of this work is, however, to provide relatively simple numerical implementations on the topic of buckling at multiple-scale levels and its connection with topology optimization of structures, as a way of smoothing out the inherent difficulties of the problems.

1.4 Thesis Outline

For the sake of readability and understanding of the involved topics, this work is divided into four main sections.

In chapter 2, the necessary theoretical background to the proposed implementations is given. This includes the layout of the used theories along with references for further details on the discussed topics.

Chapter 3 is focused on the description of the carried-out studies and numerical implementations. These include a brief review on the development of symbolic computation scripts for the derivation of

the used linearized stability theory, the extension of an existing code for the calculation of homogenized material properties, the development of computational models to obtain buckling responses at micro-, macro- and mixed-scales, the review and modification of existing codes for the compliance minimization problem with the MMA as the updating scheme for the design variables and the numerical implementation of topology optimization problems for the maximization of the linearized critical buckling load without considering the case of multiple eigenvalues.

The results from the implementations in chapter 3 are presented in chapter 4, together with some verification examples.

In chapter 5, the main conclusions of this work are summarized and some comments and reflections on futures works to be addressed are made.

Chapter 2

Theoretical Background

In this chapter, a theoretical overview of the discussed topics is given. The necessary concepts and equations for the carried-out methodology are presented, where the reader is referred to the given references for more details on the discussed subjects.

2.1 Linear elasticity equations for isotropic solids

A continuum body is said to be a linear elastic solid when, in the presence of an external force, the resultant deformation disappears as the force is removed. In the words of the elasticity theory, the stress at any material point of a linear elastic solid is only linearly dependent on the strain at that point and at that moment (here assumed independent of the history and rate of strain).

The classic equations of linear elasticity result from the following simplifications:

- Only the macroscopic structure of the body is considered - the other scales of the structure are not taken into account;
- The solid is assumed to be a continuously distributed mass over its volume, which implies that all portions of the body are assumed free of imperfections;
- The displacements and velocities are infinitesimal (small deformations) and sufficiently smooth.

In what follows, only isotropic materials - materials for which the elastic properties are the same in every direction - are treated and no thermal or viscous effects are considered.

In a linear elasticity theory, the small strain tensor is defined as

$$e_{ij} = \frac{1}{2}\left(\frac{\partial u_i}{\partial x_j} + \frac{\partial u_j}{\partial x_i}\right), \tag{2.1}$$

where $u_i(x_1, x_2, x_3, t)$ with $i = 1, 2, 3$ is the displacement component i of a point from its position in the zero-stress state (undeformed configuration) to the x_1, x_2, x_3 position at time t (deformed configuration).

The particle velocity and acceleration are, respectively,

$$v_i = \frac{\partial u_i}{\partial t},\ \alpha_i = \frac{\partial v_i}{\partial t}. \tag{2.2}$$

From the principle of mass conservation, one can obtain the continuity equation,

$$\frac{\partial \rho}{\partial t} + \frac{\partial (\rho v_i)}{\partial x_i} = 0. \tag{2.3}$$

The conservation of momentum law, or simply equation of motion, expressing the system's equilibrium of forces can be written as

$$\rho \alpha_i = \frac{\partial \sigma_{ij}}{\partial x_j} + f_i. \tag{2.4}$$

Furthermore, linear elastic bodies (Cauchy or Green) obey Hooke's law - the strains and displacements are measured from a zero value, to which a unique zero-stress state is associated. The generalized Hooke's law is $\sigma_{ij} = E_{ijkm} e_{km}$ and for a homogeneous and isotropic material, it can be particularized to $\sigma_{ij} = \lambda e_{kk} \delta_{ij} + 2\mu e_{ij}$, where λ and μ are the Lamé parameters.

The so far presented equations represent 22 equations for 22 unknowns, namely ρ, u_i, v_i, α_i, e_{ij} and σ_{ij} with i, j=1,2,3 or, alternatively, $i, j = x, y, z$ [27] .

Using equations (2.1), (2.4) and the Hooke's law for isotropic materials, σ_{ij} and e_{ij} can be eliminated and the Navier equation is obtained,

$$\mu \nabla^2 u_i + (\lambda + \mu) \frac{\partial e}{\partial x_i} + f_i = \rho \frac{\partial^2 u_i}{\partial t^2}, \tag{2.5}$$

where ∇^2 is the Laplace operator and e is the divergence of the displacement vector.

For static problems, the previous equation is reduced to

$$\mu \nabla^2 u_i + (\lambda + \mu) \frac{\partial e}{\partial x_i} + f_i = 0. \tag{2.6}$$

To solve the previous field equation, the specification of boundary conditions is necessary, which may be (usually) either displacements or surface tractions.

The demonstrations of the given relations and further details on the elasticity theory can be found in [27] or [28].

Because the developed work refers to situations that can be modeled as two-dimensional (either due to the system's geometry, boundary conditions or applied loads), only plane elasticity equations of two types are now considered:

- Plane strain in xy-plane: State of strain in which the strain normal to the xy-plane as well as the shear strains involving angles normal to the xy-plane are assumed to be zero. These assumptions are appropriate for thick structures (in the z direction) with constant cross-sectional area where the applied loads act only in the xy-plane and do not vary in the z direction.

- Plane stress in xy-plane: State of stress in which the stresses normal to the xy-plane are assumed

to be zero. This model is realistic for thin bodies (in the z direction) where external loads are only applied in the xy-plane.

Plane strain equations

For a plane strain problem, the displacement field is characterized as

$$u_1 = u_1(x_1, x_2),\ u_2 = u_2(x_1, x_2),\ u_3 = 0. \tag{2.7}$$

From the Green tensor defined above and introducing the plane strain simplifications, the strain components are

$$e_{13} = e_{23} = e_{33} = 0,\ e_{11} = \frac{\partial u_1}{\partial x_1},\ 2e_{12} = \frac{\partial u_1}{\partial x_2} + \frac{\partial u_2}{\partial x_1},\ e_{22} = \frac{\partial u_2}{\partial x_2}. \tag{2.8}$$

As for the stress components (recalling that here only isotropic materials are treated),

$$\sigma_{13} = \sigma_{23} = 0,\ \sigma_{33} = \nu\left(\sigma_{11} + \sigma_{22}\right) \tag{2.9}$$

and the constitutive equation (Hooke's law) becomes, using a matrix notation,

$$\begin{Bmatrix} \sigma_{11} \\ \sigma_{22} \\ \sigma_{12} \end{Bmatrix} = \frac{E}{(1+\nu)(1-2\nu)} \begin{bmatrix} 1-\nu & \nu & 0 \\ \nu & 1-\nu & 0 \\ 0 & 0 & \frac{1-2\nu}{2} \end{bmatrix} \begin{Bmatrix} e_{11} \\ e_{22} \\ 2e_{12} \end{Bmatrix}. \tag{2.10}$$

As for the equation of motion (2.6) for static conditions, the following system of 2 equations, written in terms of the stress components, is obtained.

$$\frac{\partial \sigma_{11}}{\partial x_1} + \frac{\partial \sigma_{12}}{\partial x_2} + f_1 = 0 \tag{2.11}$$

$$\frac{\partial \sigma_{12}}{\partial x_1} + \frac{\partial \sigma_{22}}{\partial x_2} + f_2 = 0 \tag{2.12}$$

The boundary conditions for solving the previous problem take the form of:

$$\text{Essential (displacements): } u_1 = \hat{u}_1,\ u_2 = \hat{u}_2 \text{ on } \Gamma_u \tag{2.13}$$

$$\text{Natural (tractions): } t_1 \equiv \sigma_{11} n_1 + \sigma_{12} n_2 = \hat{t}_1,\ t_2 \equiv \sigma_{12} n_1 + \sigma_{22} n_2 = \hat{t}_2 \text{ on } \Gamma_t, \tag{2.14}$$

where (n_1, n_2) represent the direction cosines of the unit normal vector on the system's boundary Γ and Γ_u and Γ_t are disjoint portions of Γ, where displacements and tractions are prescribed, respectively.

Plane stress equations

Regarding plane stress situations, only the differences between this state and the plane strain state will be outlined.

In a plane stress case, the stress field is characterized by

$$\sigma_{13} = \sigma_{23} = \sigma_{33} = 0, \tag{2.15}$$

with the remaining stress components given by the following constitutive equation.

$$\begin{Bmatrix} \sigma_{11} \\ \sigma_{22} \\ \sigma_{12} \end{Bmatrix} = \frac{E}{(1-\nu^2)} \begin{bmatrix} 1 & \nu & 0 \\ \nu & 1 & 0 \\ 0 & 0 & \frac{1-\nu}{2} \end{bmatrix} \begin{Bmatrix} e_{11} \\ e_{22} \\ 2e_{12} \end{Bmatrix} \tag{2.16}$$

Although not yet mentioned, particular attention is now given to the equations of motion, which are the same as in the plane strain case when written in terms of the stresses and not the displacements. In fact, when expressed in terms of the components of the displacement field, the inequality of the equations is a result of the difference in the constitutive equations for both cases.

Finite element formulation - plane elasticity problems

The equilibrium equations (2.11) and (2.12) describe the system's behaviour as a continuous body and therefore require a solution in every material point of the system. These equations, together with the boundary conditions, are usually referred to as the *strong formulation* of the problem.

The so called *weak formulation* is the starting point for obtaining the system's finite element model. It can be obtained by performing the integration of the equilibrium equation over each element and introducing weight/test functions $\boldsymbol{v}$. For a given element e,

$$\int_{\Omega_e} \left(\frac{\partial \sigma_{ij}}{\partial x_j} + f_i \right) v_i d\Omega = 0, \tag{2.17}$$

which leads to (see [29])

$$\int_{\Omega_e} E_{ijkm} \frac{\partial u_k}{\partial x_m} \frac{\partial v_i}{\partial x_j} d\Omega = \int_{\Omega_e} f_i v_i d\Omega + \int_{\Gamma_t} t_i v_i d\Gamma. \tag{2.18}$$

Since the primary variables are the displacements, the model is constructed by introducing the appropriate interpolation functions to approximate the displacement field. Mathematically,

$$u_1 \approx \sum_{j=1}^{n} u_1^j N_j(x_1, x_2), \; u_2 \approx \sum_{j=1}^{n} u_2^j N_j(x_1, x_2), \tag{2.19}$$

where n indicates the number of nodes per element, N the shape functions and u_i^j the nodal displacements values.

The linear equations describing the finite element model for static problems are then obtained by

the introduction of the previous approximation into the weak formulation. Using a matrix notation, these equations are outlined bellow.

$$\text{Displacement field: } \boldsymbol{u^h} = \{u_1\ u_2\}^T = \boldsymbol{N}\boldsymbol{u}. \tag{2.20}$$

$$\text{Strain field: } \boldsymbol{e} = \boldsymbol{B}\boldsymbol{u}. \tag{2.21}$$

$$\text{Stress field: } \boldsymbol{\sigma} = \boldsymbol{E}\boldsymbol{B}\boldsymbol{u}. \tag{2.22}$$

$$\text{Governing equation: } \boldsymbol{K}\boldsymbol{u} = \boldsymbol{F}. \tag{2.23}$$

The displacement field $\boldsymbol{u^h}$ is obtained by means of the nodal displacement vector

$$\boldsymbol{u} = \{u_1^1\ u_2^1\ u_1^2\ u_2^2\ ...\ u_1^n\ u_2^n\}^T \tag{2.24}$$

and the shape function matrix

$$\boldsymbol{N} = \begin{bmatrix} N_1 & 0 & N_2 & 0 & ... & N_n & 0 \\ 0 & N_1 & 0 & N_2 & ... & 0 & N_n \end{bmatrix}, \tag{2.25}$$

where n is the number of nodes per element.

The strain field is obtained using the strain-displacement matrix

$$\boldsymbol{B} = \begin{bmatrix} \frac{\partial N_1}{\partial x_1} & 0 & \frac{\partial N_2}{\partial x_1} & 0 & ... & \frac{\partial N_n}{\partial x_1} & 0 \\ 0 & \frac{\partial N_1}{\partial x_2} & 0 & \frac{\partial N_2}{\partial x_2} & ... & 0 & \frac{\partial N_n}{\partial x_2} \\ \frac{\partial N_1}{\partial x_2} & \frac{\partial N_1}{\partial x_1} & \frac{\partial N_2}{\partial x_2} & \frac{\partial N_2}{\partial x_1} & ... & \frac{\partial N_n}{\partial x_2} & \frac{\partial N_n}{\partial x_1} \end{bmatrix} \tag{2.26}$$

and the stress field, recalling Hooke's law, is obtained by means of the strain field and the constitutive matrix $\boldsymbol{E}$, which for the considered elasticity problems is either the one defined in equation (2.10) or in equation (2.16).

As for the governing equation, the global stiffness matrix $\boldsymbol{K}$ and the global force vector $\boldsymbol{F}$ are obtained from the assemblage of its elemental correspondents given, respectively, by

$$\boldsymbol{K^e} = \int_{\Omega_e} \boldsymbol{B^T}\boldsymbol{E}\boldsymbol{B}\ d\Omega, \tag{2.27}$$

$$\boldsymbol{F^e} = \int_{\Omega_e} \boldsymbol{N}^T\boldsymbol{f}\ d\Omega + \int_{\Gamma_t} \boldsymbol{N}^T\boldsymbol{t}\ d\Gamma \tag{2.28}$$

Further details on plane elasticity problems and their finite element formulation can be found, for instance, in [29] and [30].

2.2 Linear elastic buckling theory for solids with periodic micro-structure

The stability problem is here analyzed as a bifurcation in the static equilibrium displacement path of some body, where it is assumed that the only possible failing mechanism of the structure is linear elastic buckling. Furthermore, it will be also assumed that, before instability occurs, the material and geometrical behavior of the component is linear-elastic and that the sideways deflections (deflections perpendicular to the direction of the load application) are null. These hypothesis reduce the stability problem to an eigenvalue problem, also known as Euler Buckling problem.

The linear-elastic buckling theory here presented is based on [16] and [26] and the references therein.

2.2.1 Problem formulation

Let a linear-elastic body be defined by a domain Ω^ε and a boundary Γ, being quasi-statically loaded with: prescribed displacements in Γ_u, surface tractions $\boldsymbol{t}$ in Γ_t and body forces $\boldsymbol{f}$ in Ω^ε. The superscript ε, which will also be of further use in this text, indicates a dependency on the micro-structure, as it is defined as the unit cell scale parameter,

$$\varepsilon = \frac{d}{D} \ll 1, \tag{2.29}$$

where d is a characteristic dimension of the unit cell and D a characteristic dimension of the structure at the macro-scale level.

The loading is gradually increased, only applied at the macro-scale level and also considered proportional to some reference loading, $\boldsymbol{t} = \lambda \boldsymbol{t^{ref}}$ and $\boldsymbol{f} = \lambda \boldsymbol{f^{ref}}$.

Assuming the body has a uniform micro-structural shape, the solid can be represented by a periodic repetition of a unit cell, also know in the literature as RVE. The RVE is defined by the domain $Y =]0, Y_1[\text{x}]0, Y_2[\text{x}]0, Y_3[$ and, here, built from a base material with holes in it. Furthermore, this base material is homogeneous, linear-elastic and isotropic.

The buckling problem consists, then, on the determination of the critical loads and the displacement field for which instability occurs. However, because this is a linearized model, it is not possible to obtain the displacements; instead only the instability modes can be identified.

2.2.2 Obtaining a governing equation

Using the minimization of the potential energy approach to obtain the problem's governing equation, the critical load factor $\lambda = \lambda_{cr}$ as well as the instability modes can be determined.

The total potential energy is defined as

$$\Pi(\boldsymbol{u}^\varepsilon) = A(\boldsymbol{u}^\varepsilon) - R(\boldsymbol{u}^\varepsilon), \tag{2.30}$$

where $A(\boldsymbol{u}^{\boldsymbol{\varepsilon}})$ is the total elastic strain energy and $R(\boldsymbol{u}^{\boldsymbol{\varepsilon}})$ is the applied forces potential given by

$$A(\boldsymbol{u}^{\varepsilon}) = \frac{1}{2}\int_{\Omega} \sigma_{ij}(\boldsymbol{u}^{\varepsilon}) e_{ij}(\boldsymbol{u}^{\varepsilon}) d\Omega = \frac{1}{2}\int_{\Omega} E_{ijkm} e_{km}(\boldsymbol{u}^{\varepsilon}) e_{ij}(\boldsymbol{u}^{\varepsilon}) d\Omega, \tag{2.31}$$

$$R(\boldsymbol{u}^{\boldsymbol{\varepsilon}}) = \lambda \int_{\Omega} f_i^{ref} u_i^{\varepsilon} d\Omega + \lambda \int_{\Gamma_t} t_i^{ref} u_i^{\varepsilon} d\Gamma. \tag{2.32}$$

In obtaining the final expression for the elastic strain energy, the material behavior was, as stated before, presumed elastic, not excluding geometric nonlinearities. Therefore, the stress-strain relation can be given by the generalized Hooke's law $\sigma_{ij}(\boldsymbol{u}^{\boldsymbol{\varepsilon}}) = E_{ijkm} e_{km}(\boldsymbol{u}^{\boldsymbol{\varepsilon}})$.

In contrast with the linear elasticity theory, the second order terms in the Green strain tensor (geometric terms) cannot be neglected, as these are the ones that cause the vanishing of the structure's stiffness as it buckles. The Green strain tensor is then expressed as

$$e_{ij}(\boldsymbol{u}^{\varepsilon}) = \frac{1}{2}\left(\frac{\partial u_i^{\varepsilon}}{\partial x_j} + \frac{\partial u_j^{\varepsilon}}{\partial x_i}\right) + \frac{1}{2}\left(\frac{\partial u_k^{\varepsilon}}{\partial x_i}\frac{\partial u_k^{\varepsilon}}{\partial x_j}\right). \tag{2.33}$$

The displacement field, which is a function of both the macro-spatial, $\boldsymbol{x}$, and micro-spatial, $\boldsymbol{y}$, variables, is represented using an infinitesimal real displacement parameter α:

$$\boldsymbol{u}^{\varepsilon} = \boldsymbol{u}^{0\varepsilon} + \alpha \boldsymbol{u}^{1\varepsilon}. \tag{2.34}$$

In the previous expression, $\boldsymbol{u}^{\boldsymbol{0\varepsilon}}$ is the displacement related with the primary equilibrium configuration (unique solution of the linear elastic problem before bifurcation and assumed known) and $\boldsymbol{u}^{\boldsymbol{1\varepsilon}}$ is a relative displacement which, when multiplied by α, represents the possible "jump" to the secondary equilibrium position that occurs when bifurcation takes place.

Introducing the above displacement representation (2.34) in the strain tensor (2.33) yields

$$e_{ij}(\boldsymbol{u}^{\varepsilon}) = \frac{1}{2}\left(\frac{\partial u_i^{0\varepsilon}}{\partial x_j} + \frac{\partial u_j^{0\varepsilon}}{\partial x_i}\right) + \frac{1}{2}\left(\frac{\partial u_k^{0\varepsilon}}{\partial x_i}\frac{\partial u_k^{0\varepsilon}}{\partial x_j}\right) +$$

$$+ \alpha\left\{\frac{1}{2}\left(\frac{\partial u_i^{1\varepsilon}}{\partial x_j} + \frac{\partial u_j^{1\varepsilon}}{\partial x_i}\right) + \frac{1}{2}\left(\frac{\partial u_k^{0\varepsilon}}{\partial x_i}\frac{\partial u_k^{1\varepsilon}}{\partial x_j} + \frac{\partial u_k^{1\varepsilon}}{\partial x_i}\frac{\partial u_k^{0\varepsilon}}{\partial x_j}\right)\right\} + \alpha^2\left\{\frac{1}{2}\frac{\partial u_k^{1\varepsilon}}{\partial x_i}\frac{\partial u_k^{1\varepsilon}}{\partial x_j}\right\}. \tag{2.35}$$

Given the assumption that the deformations occurring before the bifurcation $\boldsymbol{u}^{\boldsymbol{0\varepsilon}}$ are infinitesimal, the second order term $\left(\frac{\partial u_k^{0\varepsilon}}{\partial x_i}\frac{\partial u_k^{0\varepsilon}}{\partial x_j}\right)$ can be neglected when compared to its first order correspondent. The nonlinear crossed terms $\left(\frac{\partial u_k^{0\varepsilon}}{\partial x_i}\frac{\partial u_k^{1\varepsilon}}{\partial x_j} + \frac{\partial u_k^{1\varepsilon}}{\partial x_i}\frac{\partial u_k^{0\varepsilon}}{\partial x_j}\right)$ are also negligible, since $\boldsymbol{u}^{0\varepsilon}$ and $\boldsymbol{u}^{1\varepsilon}$ do not coexist in any of the equilibrium configurations. The small deformations assumption and its mentioned consequences is what linearizes the buckling problem, reducing it to a eigenvalue problem.

With these simplifications, the Green strain tensor becomes

$$e_{ij}(\boldsymbol{u}^{\varepsilon}) = \frac{1}{2}\left(\frac{\partial u_i^{0\varepsilon}}{\partial x_j} + \frac{\partial u_j^{0\varepsilon}}{\partial x_i}\right) + \alpha\left\{\frac{1}{2}\left(\frac{\partial u_i^{1\varepsilon}}{\partial x_j} + \frac{\partial u_j^{1\varepsilon}}{\partial x_i}\right)\right\} + \alpha^2\left\{\frac{1}{2}\frac{\partial u_k^{1\varepsilon}}{\partial x_i}\frac{\partial u_k^{1\varepsilon}}{\partial x_j}\right\}. \tag{2.36}$$

As in many other problems in mechanics, the bifurcation problem is here addressed by means of an

asymptotic technique, which allows to obtain:

- A two-scale linear-elastic buckling theory;
- Homogenized elastic material properties, which can be used when treating the macro-scale instability problem, assuming that periodicity exists at the microscopic level.

Expanding the displacement field terms defined in (2.34) yields

$$\boldsymbol{u}^{0\varepsilon}(\boldsymbol{x},\boldsymbol{y}) = \boldsymbol{u}^{00}(\boldsymbol{x},\boldsymbol{y}) + \varepsilon\boldsymbol{u}^{01}(\boldsymbol{x},\boldsymbol{y}) + \varepsilon^2\boldsymbol{u}^{02}(\boldsymbol{x},\boldsymbol{y}) + ...,\ \boldsymbol{y} = \frac{\boldsymbol{x}}{\varepsilon}, \tag{2.37}$$

$$\boldsymbol{u}^{1\varepsilon}(\boldsymbol{x},\boldsymbol{y}) = \boldsymbol{u}^{10}(\boldsymbol{x},\boldsymbol{y}) + \varepsilon\boldsymbol{u}^{11}(\boldsymbol{x},\boldsymbol{y}) + \varepsilon^2\boldsymbol{u}^{12}(\boldsymbol{x},\boldsymbol{y}) + ...,\ \boldsymbol{y} = \frac{\boldsymbol{x}}{\varepsilon}, \tag{2.38}$$

where the functions $\boldsymbol{u}^{ab}$ with indices a=0,1 and b=0,1,2,... are Y-periodic (have the same periodicity as the unit cell).

Given that the differentiation of Y-periodic functions $F(\boldsymbol{x},\boldsymbol{y})$ can be performed as [26]

$$\frac{d}{dx_j}F(\boldsymbol{x},\boldsymbol{y}) = \frac{\partial F(\boldsymbol{x},\boldsymbol{y})}{\partial x_j} + \frac{1}{\varepsilon}\frac{\partial F(\boldsymbol{x},\boldsymbol{y})}{\partial y_j} \tag{2.39}$$

and presenting the results writing only the first two terms of the asymptotic expansions (2.37) and (2.38) (which is reasonable, when recalling that the scale parameter ε is much lower than unity), the strain-displacement relation becomes

$$e_{ij}(\boldsymbol{u}^{\varepsilon}) = e^0_{ij}(\boldsymbol{u}^{\varepsilon}) + \alpha e^I_{ij}(\boldsymbol{u}^{\varepsilon}) + \alpha^2 e^{II}_{ij}(\boldsymbol{u}^{\varepsilon}), \tag{2.40}$$

where

$$e^0_{ij}(\boldsymbol{u}^{\varepsilon}) = \frac{1}{2\varepsilon}\left(\frac{\partial u^{00}_i}{\partial y_j} + \frac{\partial u^{00}_j}{\partial y_i}\right) + \left[\frac{1}{2}\left(\frac{\partial u^{00}_i}{\partial x_j} + \frac{\partial u^{00}_j}{\partial x_i}\right) + \frac{1}{2}\left(\frac{\partial u^{01}_i}{\partial y_j} + \frac{\partial u^{01}_j}{\partial y_i}\right)\right] + \frac{\varepsilon}{2}\left(\frac{\partial u^{01}_i}{\partial x_j} + \frac{\partial u^{01}_j}{\partial x_i}\right) + ..., \tag{2.41}$$

$$e^I_{ij}(\boldsymbol{u}^{\varepsilon}) = \frac{1}{2\varepsilon}\left(\frac{\partial u^{10}_i}{\partial y_j} + \frac{\partial u^{10}_j}{\partial y_i}\right) + \left[\frac{1}{2}\left(\frac{\partial u^{10}_i}{\partial x_j} + \frac{\partial u^{10}_j}{\partial x_i}\right) + \frac{1}{2}\left(\frac{\partial u^{11}_i}{\partial y_j} + \frac{\partial u^{11}_j}{\partial y_i}\right)\right] + \frac{\varepsilon}{2}\left(\frac{\partial u^{11}_i}{\partial x_j} + \frac{\partial u^{11}_j}{\partial x_i}\right) + ..., \tag{2.42}$$

$$\begin{aligned} e^{II}_{ij}(\boldsymbol{u}^{\varepsilon}) = {} & \frac{1}{2\varepsilon^2}\left(\frac{\partial u^{10}_k}{\partial y_i}\frac{\partial u^{10}_k}{\partial y_j}\right) + \frac{1}{2\varepsilon}\left(\frac{\partial u^{10}_k}{\partial x_i}\frac{\partial u^{10}_k}{\partial y_j} + \frac{\partial u^{10}_k}{\partial y_i}\frac{\partial u^{10}_k}{\partial x_j} + \frac{\partial u^{10}_k}{\partial y_i}\frac{\partial u^{11}_k}{\partial y_j} + \frac{\partial u^{11}_k}{\partial y_i}\frac{\partial u^{10}_k}{\partial y_j}\right) + \\ & + \frac{1}{2}\left(\frac{\partial u^{10}_k}{\partial x_i}\frac{\partial u^{10}_k}{\partial x_j} + \frac{\partial u^{10}_k}{\partial x_i}\frac{\partial u^{11}_k}{\partial y_j} + \frac{\partial u^{11}_k}{\partial y_i}\frac{\partial u^{10}_k}{\partial x_j} + \frac{\partial u^{10}_k}{\partial y_i}\frac{\partial u^{11}_k}{\partial x_j} + \frac{\partial u^{11}_k}{\partial x_i}\frac{\partial u^{10}_k}{\partial y_j} + \frac{\partial u^{11}_k}{\partial y_i}\frac{\partial u^{11}_k}{\partial y_j}\right) + \\ & + \frac{\varepsilon}{2}\left(\frac{\partial u^{11}_k}{\partial y_i}\frac{\partial u^{11}_k}{\partial x_j} + \frac{\partial u^{11}_k}{\partial x_i}\frac{\partial u^{11}_k}{\partial y_j} + \frac{\partial u^{11}_k}{\partial x_i}\frac{\partial u^{10}_k}{\partial x_j} + \frac{\partial u^{10}_k}{\partial x_i}\frac{\partial u^{11}_k}{\partial x_j}\right) + \frac{\varepsilon^2}{2}\left(\frac{\partial u^{11}_k}{\partial x_i}\frac{\partial u^{11}_k}{\partial x_j}\right) + ... \,. \end{aligned} \tag{2.43}$$

The minimization of the total potential energy, which is related with the equilibrium configurations, is expressed by its stationary points,

$$\delta\Pi(\boldsymbol{u}^{\varepsilon}) = \delta A(\boldsymbol{u}^{\varepsilon}) - \delta R(\boldsymbol{u}^{\varepsilon}) = 0. \tag{2.44}$$

Introducing a perturbation $\delta u^{\varepsilon} = \alpha\{\boldsymbol{v}^{10}(\boldsymbol{x},\boldsymbol{y}) + \varepsilon\boldsymbol{v}^{11}(\boldsymbol{x},\boldsymbol{y}) + ...\}$, where $\boldsymbol{v}^{10}$ and $\boldsymbol{v}^{11} \in V_{\Omega\times Y} = \{\boldsymbol{v}(\boldsymbol{x},\boldsymbol{y}) : \boldsymbol{v}|_{\Gamma_u} = 0$ and $\boldsymbol{v}$ is Y-periodic$\}$ and using the so far obtained strain tensor, the previous equation

can be separated in terms of α powers:

$$\alpha \int_{\Omega^\varepsilon} E_{ijkm}\{e^0_{ij}(\boldsymbol{u}^\varepsilon)e^I_{km}(\boldsymbol{v}^\varepsilon)\}d\Omega - \alpha\lambda \int_{\Gamma_t} \boldsymbol{t}_i \boldsymbol{v}_i^\varepsilon d\Gamma - \alpha\lambda \int_{\Omega^\varepsilon} \boldsymbol{f}_i \boldsymbol{v}_i^\varepsilon d\Omega = 0 \;\forall\; \boldsymbol{v} \in V_{\Omega\times Y}, \tag{2.45}$$

$$\alpha^2 \int_{\Omega^\varepsilon} E_{ijkm}\{e^0_{ij}(\boldsymbol{u}^\varepsilon)e^{II}_{km}(\boldsymbol{v}^\varepsilon) + e^0_{ij}(\boldsymbol{v}^\varepsilon)e^{II}_{km}(\boldsymbol{u}^\varepsilon) + e^I_{ck}(\boldsymbol{u}^\varepsilon)e^I_{cm}(\boldsymbol{v}^\varepsilon) + e^I_{ck}(\boldsymbol{v}^\varepsilon)e^I_{cm}(\boldsymbol{u}^\varepsilon)\}d\Omega = 0 \;\forall\; \boldsymbol{v} \in V_{\Omega\times Y}. \tag{2.46}$$

Note: In equations (2.45) and (2.46) some terms were omitted as $e^0_{ij}(\boldsymbol{v}^\varepsilon) = 0$, because the solution is unique before the bifurcation, and $e^0_{ij}(\boldsymbol{u}^\varepsilon)e^I_{km}(\boldsymbol{u}^\varepsilon) = 0$ due to the fact that the displacements $\boldsymbol{u}^{0\varepsilon}$ and $\boldsymbol{u}^{1\varepsilon}$ do not coexist at bifurcation.

2.2.3 Pre-buckling response

The equations that characterize the small elastic deformations occurring before buckling of a solid built from a periodic micro-structure are obtained from the analysis of equation (2.45) - the α term of the total potential energy stationary condition. The analysis is performed by grouping the terms in ε powers and setting each of them to zero. With this approach, three sets of equations are obtained:

- The equations describing the linear-elastic fundamental equilibrium configuration at the micro-scale level;
- The equations describing the linear-elastic fundamental equilibrium configuration at the macro-scale level;
- The equations for determining the effective elastic material properties.

These equations are outlined in what follows.

From the term in ε^{-2}, it can be shown that

$$\boldsymbol{u}^{00}(\boldsymbol{x},\boldsymbol{y}) = \boldsymbol{u}^{00}(\boldsymbol{x}), \tag{2.47}$$

meaning that the first term of the asymptotic expansion of the displacement $\boldsymbol{u}^{0\varepsilon}$ is a function of only the macro-scale spatial variable $\boldsymbol{x}$.

Analysing the term in ε^{-1} and acknowledging that $\boldsymbol{v}$ are independent variations that can assume any value, it can be obtained

$$\frac{1}{\varepsilon}\int_{\Omega^\varepsilon} E_{ijkm}\left(\frac{\partial u_i^{00}}{\partial x_j} + \frac{\partial u_i^{01}}{\partial y_j}\right)\frac{\partial v_k^{10}}{\partial y_m}d\Omega = 0,\; \forall\; \boldsymbol{v}^{10} \in V_{\Omega\times Y}. \tag{2.48}$$

Recalling that ε is very small and also that $\boldsymbol{u}^{00}$, $\boldsymbol{u}^{01}$ and $\boldsymbol{v}^{10}$ are periodic functions in $\boldsymbol{y}$, equation (2.48) can be written as

$$\int_{\Omega^\varepsilon}\left[\frac{1}{|Y|}\int_Y E_{ijkm}\left(\frac{\partial u_i^{00}}{\partial x_j} + \frac{\partial u_i^{01}}{\partial y_j}\right)\frac{\partial v_k^{10}}{\partial y_m}dY\right]d\Omega = 0,\; \forall\; \boldsymbol{v}^{10} \in V_{\Omega\times Y}. \tag{2.49}$$

where $|Y|$ represents the geometrical volume of the RVE.

Using (2.47) together with the previous result,

$$\boldsymbol{u}_i^{01}(\boldsymbol{x},\boldsymbol{y}) = -\chi_i^{km}(\boldsymbol{y})\frac{\partial u_k^{00}(\boldsymbol{x})}{\partial x_m}. \tag{2.50}$$

To satisfy the previous equation, the characteristic displacements χ_i^{km} must be the solution of the km static problems at micro-scale level,

$$\int_Y E_{ijpq}\frac{\partial \chi_i^{km}}{\partial y_q}\frac{\partial v_i}{\partial y_j}dY = \int_Y E_{ijkm}\frac{\partial v_i}{\partial y_j}dY,\ \forall\ \boldsymbol{v} \in V_Y = \{\boldsymbol{v} \text{ is Y-periodic}\}, \tag{2.51}$$

where periodic displacements at the RVE boundary are prescribed. Because χ_p^{km} takes the meaning of characteristic displacements, then the previous equation is referred to as the characteristic equation of the unit cell.

As for the term in ε^0, using the result from equation (2.50) and keeping in mind that $\boldsymbol{v}$ are arbitrary variations, ε is infinitesimal and that the functions being integrated are Y-periodic, the equation expressing macroscopic static equilibrium is obtained,

$$\int_{\Omega^\varepsilon}\frac{1}{|Y|}\int_Y\left(E_{ijkm} - E_{ijpq}\frac{\partial \chi_p^{km}}{\partial y_q}\right)dY\frac{\partial u_k^{00}}{\partial x_m}\frac{\partial v_i^{10}}{\partial x_j}d\Omega = \lambda\int_{\Gamma_t} t_i^{ref}v_i^{10}d\Gamma + \lambda\int_{\Omega^\varepsilon} f_i^{ref}v_i^{10}d\Omega,\ \forall\ \boldsymbol{v}^{10} \in V_\Omega, \tag{2.52}$$

from where the macroscopic displacements $\boldsymbol{u}^{00}$ can be determined.

From 2.52, the homogenized elastic material properties can be defined as

$$E_{ijkm}^H = \frac{1}{|Y|}\int_Y\left(E_{ijkm} - E_{ijpq}\frac{\partial \chi_p^{km}}{\partial y_q}\right)dY. \tag{2.53}$$

One can see that for the determination of the effective properties, the micro-scale equilibrium problem must be first solved. Therefore, the macroscopic static problem must be addressed after the microscopic one. Furthermore, it is clear that the solution for both the static problems does not involve the coupling of them, allowing them to be solved separately.

From the term in ε, it is possible to realize that the second term in the asymptotic expansion of $\boldsymbol{u}^{00}$, $\boldsymbol{u}^{01}$, is a function of only $\boldsymbol{y}$,

$$\boldsymbol{u}^{01}(\boldsymbol{x},\boldsymbol{y}) = \boldsymbol{u}^{01}(\boldsymbol{y}). \tag{2.54}$$

This concludes the characterization of the body behavior prior to buckling at both scale levels, which can also be identified as the solution of the homogenization problem at the micro-scale level and the solution of the static-elastic problem at the macro-scale level.

Some notes on the homogenization theory

Although the equations for the application of the homogenization theory are naturally obtained with this linear elastic buckling theory for solids with periodic micro-structure, further details and comments

on it seem appropriate.

The homogenization theory is a RVE-based method that can be used to compute effective elastic properties of composite materials. The behaviour of these materials depends on their micro-structure, which requires their analysis on a micro-scale level. The goal of the RVE-based methods is, then, to obtain valid macro-scale material properties (effective properties), based on information of a volume that represents the material (due to periodicity, etc.).

The homogenization theory is built from two main assumptions:

- Given the presence of a micro-structure, the fields of interest vary on multi-spatial levels;

- A periodic spatial repetition of a micro-structure exists.

Furthermore, it has been shown that the accuracy of the homogenization procedure depends on ε - as ε decreases, the resultant effective material behavior is closer to the one of the "true" material [17]. The common use of periodic boundary conditions when applying this method is also justified by being the ones that enable the best agreement with experimental results [17].

In this theory, the relevant field variables are represented by their asymptotic expansions, as done in equations (2.37) and (2.38), resulting in an asymptotic representation of the governing equations. This technique is what allows the spatial scale separation of the problem where homogenization is applied.

When applied to elasticity problems, this analysis enables the calculation of the effective macroscopic elasticity tensor from

$$E^H_{ijkl} = \frac{1}{|Y|}\int_Y E_{pqrs}\left(\tilde{\varepsilon}^{ij}_{pq} - \varepsilon^{ij}_{pq}\right)\left(\tilde{\varepsilon}^{kl}_{rs} - \varepsilon^{kl}_{rs}\right) dY, \tag{2.55}$$

where $\tilde{\varepsilon}^{ij}_{pq}$ are the macroscopic strain fields (three in two-dimensional analysis) to which the unit cell is subjected and ε^{ij}_{pq} are denoted as the locally varying strain fields defined as $\varepsilon^{ij}_{pq} = \left(\frac{\partial \chi_p^{ij}}{\partial y_q} + \frac{\partial \chi_q^{ij}}{\partial y_p}\right)$ [1].

Note: Equation (2.55) is the equivalent energy based form of equation 2.53 and they both provide the same results [1].

The prescribed macroscopic strain fields are usually applied as unit independent strain fields (although any independent strain fields would also be applicable), since their linear combination can result in the macroscopic/average strain tensor. This is done, because the macroscopic strain field is not known and it is valid, since the homogenization analysis represents a linear problem [17].

The characteristic displacement fields χ^{ij}_q are the solution of the microscopic static problem (equation (2.51)), also expressed by

$$\int_Y E_{ijpq}\varepsilon_{ij}(v)\varepsilon_{pq}(\chi^{kl})dY = \int_Y E_{ijpq}\varepsilon_{ij}(v)\tilde{\varepsilon}^{kl}_{pq}dY,\ \forall v \in V_Y. \tag{2.56}$$

Further theoretical details on the homogenization theory can be found, for instance, in [31] and, as a final note, it is important to mention that due to the periodicity assumption, the obtained material properties are independent of the unit cell's size.

Finite element formulation

In problem (2.52), $\boldsymbol{u}^{00}$ depends linearly of the load factor λ. Then, one can write $\boldsymbol{u}^{00} = \lambda \boldsymbol{u}$, where $\boldsymbol{u}$ is the displacement field associated with the reference loading that solves the linear system of equilibrium equations [26]

$$\int_{\Omega^\varepsilon} E^H_{ijkm} \frac{\partial u_k}{\partial x_m} \frac{\partial v_i}{\partial x_j} d\Omega = \int_{\Gamma_t} t_i^{ref} v_i d\Gamma + \int_{\Omega^\varepsilon} f_i^{ref} v_i d\Omega, \ \forall \ \boldsymbol{v} \in V_\Omega, \tag{2.57}$$

The use of the finite element method to solve the equilibrium equation (2.57) for $\boldsymbol{u}$ requires the discretization of the domain Ω^ε in some type of finite elements and the introduction of approximation functions so that the displacement field in each element is interpolated using its nodal values.

Introducing this approximation in the governing equation, yields the following system of linear equations

$$\boldsymbol{K_x u} = \boldsymbol{F_x}, \tag{2.58}$$

where $\boldsymbol{K_x}$ is the macro-scale stiffness matrix of the structure with homogenized material properties and $\boldsymbol{F_x}$ is the applied loads vector at macroscopic level.

In a practical way, this is the same approach (and the same problem) as the one presented in the linear-elasticity chapter, taking only into consideration that the constitutive matrix is now a homogenized one. This means that the stiffness matrix, the strains and stresses can be calculated by the same matrix products there outlined, substituting only the elastic constants by the homogenized ones.

The same goes for the micro-structure elastic-static problem, where the characteristic displacements, are obtained by solving the km linear systems

$$\boldsymbol{K_y} \boldsymbol{\chi}^{km} = \boldsymbol{F_y}^{km}, \tag{2.59}$$

with $\boldsymbol{K_y}$ being the stiffness matrix related with the RVE and $\boldsymbol{F_y}^{km}$ the characteristic loading at micro-scale level. Here, the constitutive matrix is the one of the base material for elements not corresponding to the micro-structure holes. This equation represents 3 systems of equations ($km = 11, 12, 22$) in two-dimensional situations (with 3 different loadings) and, as mentioned before, they are solved considering periodic displacement boundary conditions.

From the solution of the previous equation, the homogenized constitutive matrix can be obtained as follows [1]

$$\boldsymbol{E}^H_{ij} = \frac{1}{|Y|} \sum_{e=1}^{N} \int_{Y_e} \left(\tilde{\boldsymbol{\varepsilon}}^i - \boldsymbol{B}_e \boldsymbol{\chi}_e^i \right)^T \boldsymbol{E}_e \left(\tilde{\boldsymbol{\varepsilon}}^j - \boldsymbol{B}_e \boldsymbol{\chi}_e^j \right) dY, \tag{2.60}$$

where $\boldsymbol{E}_e$ is the constitutive matrix of the material to which the element refers to, $\tilde{\varepsilon}_i^j = \delta_{ij}$ are 3 independent macroscopic strain fields and $\boldsymbol{\chi}_e$ are the correspondent 3 characteristic displacement fields. Here, the sum has the meaning of a finite element assembly procedure, where e refers to some element and N denotes the total number of elements used to discretize the unit cell.

For a comprehensive discussion on the application of finite element formulations to the homogenization problem see [32].

2.2.4 Linearized elastic buckling response

In this subsection, the second equation regarding the minimization of the total potential energy (the one in α^2 power) is addressed. The analysis of the α^2 term (2.46) is performed in the same fashion as in the previous subsection - analysing the terms in different ε powers.

Here, it will be obtained:

- The equations describing the elastic stability problem at the microscopic level;
- The equations that characterize coupled macroscopic and microscopic instabilities;
- The equations addressing the macroscopic buckling problem.

Starting with the term in ε^{-2}, an expression relating the displacement terms appearing after bifurcation and the ones that solve the linear static problem is obtained. Considering $\boldsymbol{u}^{10}(\boldsymbol{x},\boldsymbol{y}) = \boldsymbol{u}^{10}(\boldsymbol{y})$ and taking into account the periodicity of the displacements, the elastic stability problem at the micro-scale level can be obtained:

$$\int_{\#Y} E_{ijkm}\frac{\partial u_i^{10}}{\partial y_j}\frac{\partial v_k^{10}}{\partial y_m}dY + \int_{\#Y}\sigma_{km}^0\frac{\partial u_c^{10}}{\partial y_k}\frac{\partial v_c^{10}}{\partial y_m}dY = 0,\ \forall\ \boldsymbol{v}^{10}\in V_{\Omega\times\#Y}, \tag{2.61}$$

where $\sigma_{km}^0 = \sigma_{km}^0(\boldsymbol{x},\boldsymbol{y})$ is the initial stress at micro-scale level resulting from the macroscopic strain field prior to bifurcation and is defined as [1]

$$\sigma_{ij}^0 = \left(E_{ijkm} - E_{ijpq}\frac{\partial\chi_p^{km}}{\partial y_q}\right)\frac{\partial u_i^{00}}{\partial x_j}. \tag{2.62}$$

Note: The symbol # denotes periodicity in #x# RVE's, which can still be seen as Y-periodicity.

Equating the term in ε^{-1}, given that the variations $\boldsymbol{v}$ are arbitrary, a new expression of the connection between the macroscopic and microscopic instabilities is obtained:

$$\begin{aligned}&\frac{1}{\varepsilon}\int_{\Omega^\varepsilon} E_{ijkm}\left(\frac{\partial u_i^{10}}{\partial y_j}\frac{\partial v_k^{10}}{\partial x_m}\right)d\Omega + \frac{1}{\varepsilon}\int_{\Omega^\varepsilon}\sigma_{km}^0\left(\frac{\partial u_c^{10}}{\partial y_m}\frac{\partial v_c^{10}}{\partial x_k}\right)d\Omega+\\ &+\frac{1}{\varepsilon}\int_{\Omega^\varepsilon} E_{ijkm}\left(\frac{\partial u_i^{10}}{\partial x_j}\frac{\partial v_k^{10}}{\partial y_m}\right)d\Omega + \frac{1}{\varepsilon}\int_{\Omega^\varepsilon}\sigma_{km}^0\left(\frac{\partial u_c^{10}}{\partial x_k}\frac{\partial v_c^{10}}{\partial y_m}\right)d\Omega = 0,\ \forall\ \boldsymbol{v}^{10}\in V_{\Omega\times Y},\end{aligned} \tag{2.63}$$

meaning, in this case, that $\boldsymbol{u}^{10} = \boldsymbol{u}^{10}(\boldsymbol{x},\boldsymbol{y})$, i.e. a function of the macro-scale space x and micro-scale space y.

As for the term in ε^0, taking into consideration the arbitrariness of $\boldsymbol{v}$, $\boldsymbol{u}^{01} = \boldsymbol{u}^{01}(\boldsymbol{y})$ and that $\varepsilon\to 0$ and assuming $\boldsymbol{u}^{10} = \boldsymbol{u}^{10}(\boldsymbol{x})$ and that terms involving the product of three displacement derivatives may be neglected, one concludes that

$$u_i^{11}(\boldsymbol{x},\boldsymbol{y}) = -\chi_i^{km}(\boldsymbol{y})\frac{\partial u_k^{10}(\boldsymbol{x})}{\partial x_m}. \tag{2.64}$$

Making use of another variation in ε^0 and considering the same results and assumptions as in the previous paragraph, the macroscopic instability problem is obtained

$$\int_{\Omega^\varepsilon} E^H_{ijkm} \frac{\partial u_i^{10}}{\partial x_j} \frac{\partial v_k^{10}}{\partial x_m} d\Omega + \int_{\Omega^\varepsilon} \sigma^{0H}_{km} \frac{\partial u_c^{10}}{\partial x_k} \frac{\partial v_c^{10}}{\partial x_m} d\Omega = 0 \; \forall \, \boldsymbol{v}^{10} \in V_{\Omega \times Y}, \tag{2.65}$$

where

$$\sigma^{0H}_{ij} = \frac{1}{|Y|} \int_Y \left(E_{ijkm} - E_{ijpq} \frac{\partial \chi_p^{km}}{\partial y_q} \right) dY \frac{\partial u_i^{00}}{\partial x_j} = E^H_{ijkm} \frac{\partial u_i^{00}}{\partial x_j}. \tag{2.66}$$

Finite element formulation

As already mentioned, one can write $\boldsymbol{u}^{00} = \lambda \boldsymbol{u}$, where $\boldsymbol{u}$ solves equation (2.57). Therefore, and since $\boldsymbol{u}^{10} = c^{te} \boldsymbol{\phi}$ and $\boldsymbol{v}^{10} = c^{te} \boldsymbol{\psi}$, where $\boldsymbol{\phi}$ denotes the instability modes and $\boldsymbol{\psi}$ the virtual instability modes (test functions), equations (2.61), (2.62), (2.65) and (2.66) can be rewritten, respectively, as

$$\int_{\#Y} E_{ijkm} \frac{\partial \phi_i}{\partial y_j} \frac{\partial \psi_k}{\partial y_m} dY + \lambda_y \int_{\#Y} \sigma^0_{km} \frac{\partial \phi_c}{\partial y_k} \frac{\partial \psi_c}{\partial y_m} dY = 0, \; \forall \, \boldsymbol{\psi} \in V_{\Omega \times \#Y}, \tag{2.67}$$

$$\sigma^0_{ij} = \left(E_{ijkm} - E_{ijpq} \frac{\partial \chi_p^{km}}{\partial y_q} \right) \frac{\partial u_i}{\partial x_j}, \tag{2.68}$$

$$\int_{\Omega^\varepsilon} E^H_{ijkm} \frac{\partial \phi_i}{\partial x_j} \frac{\partial \psi_k}{\partial x_m} d\Omega + \lambda_x \int_{\Omega^\varepsilon} \sigma^{0H}_{km} \frac{\partial \phi_c}{\partial x_k} \frac{\partial \psi_c}{\partial x_m} d\Omega = 0 \; \forall \, \boldsymbol{\psi} \in V_{\Omega \times Y}. \tag{2.69}$$

$$\sigma^{0H}_{ij} = E^H_{ijkm} \frac{\partial u_i}{\partial x_j}, \tag{2.70}$$

where λ_y and λ_x denote the load factors (eigenvalues) at the micro- and macro-scales, respectively.

The finite element formulation for the calculation of $\boldsymbol{u}$, including the one for obtaining the necessary homogenized material properties and characteristic displacements, have already been provided in the previous section.

For the stability problem of the micro-structure, the application of the finite element approximation to the instability modes leads to the system of equations

$$\left(\boldsymbol{K_y} + \lambda_y \boldsymbol{G_y} \right) \boldsymbol{\phi} = 0, \tag{2.71}$$

where $\boldsymbol{G_y}$ is the geometric stiffness matrix (also referred to as the initial stress stiffness matrix) for the unit cell. $\boldsymbol{G_y}$ is obtained from the second integral in equation (2.67) and further details on obtaining it can be found in Appendix A.

In the same way, for the macro-scale case, it is obtained

$$\left(\boldsymbol{K_x} + \lambda_x \boldsymbol{G_x} \right) \boldsymbol{\phi} = 0, \tag{2.72}$$

where $\boldsymbol{G_x}$ is the geometric stiffness matrix at the macro-scale level, obtained from the second integral in equation (2.69) and also further explained in Appendix A.

2.3 Topology optimization

The topology optimization method acts on the material distribution (within a prescribed design domain) to generate structures without assuming any preconceived shape [19]. This optimization approach makes use of the Finite Element Method to express the objective function (function used to classify the design [23]) as well as the constraint functions (such as design constraints, equilibrium equation, etc.), discretizing the design domain into finite elements.

Here, the theoretical background behind the application of the referred method to the compliance minimization problem of statically loaded structures is first considered, followed by its application for structural maximization of the (macro-scale) buckling strength. As in the previous chapters, only structures built from linear-elastic materials are discussed.

2.3.1 Topology optimization for compliance minimization of static problems

The application of topology optimization to statically loaded structures is usually formulated as the problem of finding the material distribution that minimizes the deformation of a structure subjected to a certain static loading condition. Typically, the work done by the external forces, also known in the literature as *compliance*, is used as a measure of deformation.

The minimum compliance optimization problem (with constraints on the material volume and equilibrium equation) can then be formulated as [33]

$$\begin{aligned}
\text{find}: \quad & \mathbf{x} && \text{(design variables)} \\
\text{minimize}: \quad & c(\mathbf{x}) = \boldsymbol{F}^T \boldsymbol{U}(\mathbf{x}) && \text{(objective function)} \\
\text{subject to}: \quad & \boldsymbol{g}(\mathbf{x}) = \frac{V(\mathbf{x})}{V_0} - f' \leq 0 && \text{(constraint function - volume)} \\
& \boldsymbol{K}(\mathbf{x})\boldsymbol{U}(\mathbf{x}) = \boldsymbol{F} && \text{(constraint function - equilibrium equation)} \\
& \mathbf{x}_{min} \leq \mathbf{x} \leq \mathbf{1} && \text{(constraint on the design)},
\end{aligned} \tag{2.73}$$

where $\mathbf{x}$ is the vector containing the elemental design variables, c is the compliance, V is the material volume, V_0 is the design domain volume, f' is the maximum allowed total volume fraction, $\boldsymbol{K}$ is the global stiffness matrix, $\boldsymbol{F}$ is the global force vector (independent of the design variables) and $\boldsymbol{U}$ is the global displacement vector. The system $\boldsymbol{KU} = \boldsymbol{F}$ includes boundary conditions.

Here, a *density-based approach*, namely a modified version of the Solid Isotropic Material with Penalization (SIMP) method [34] is used, where the design variables are the elemental material densities x_e and the element e Young's modulus is determined by x_e.

This modified SIMP curve is given by

$$E_e = E_e(x_e) = E_0 + x_e^p(E_1 - E_0),\ x_e \in [0, 1], \tag{2.74}$$

where E_1 is the Young's modulus of the solid material, E_0 is the "void's" Young's modulus (very small quantity in order to prevent the singularity of the stiffness matrix) and p is the penalization factor ($p > 1$

and typically $p = 3$ [35]).

Taking into account the SIMP interpolation, the elemental constitutive matrix, from the generalized Hooke's law, for isotropic materials and expressed in terms of the plane stress equations becomes

$$\boldsymbol{E}_e(x_e) = E_e(x_e)\boldsymbol{E}_{0e}, \tag{2.75}$$

where $\boldsymbol{E}_{0e}$ is the constitutive matrix for an element with unitary Young's modulus given by

$$\boldsymbol{E}_{0e} = \frac{1}{(1-\nu^2)}\begin{bmatrix} 1 & \nu & 0 \\ \nu & 1 & 0 \\ 0 & 0 & \frac{1-\nu}{2} \end{bmatrix}. \tag{2.76}$$

From this, one concludes that the stiffness matrix of element e is obtained by

$$\boldsymbol{K}_e(x_e) = E_e(x_e)\boldsymbol{K}_{0e}, \tag{2.77}$$

where $\boldsymbol{K}_{0e}$ is the stiffness matrix for an element with unit Young's modulus, which can still be calculated by equation (2.27), provided that the constitutive matrix is, in this case, $\boldsymbol{E}_{0e}$.

As usually done when using the Finite Element Method, the global stiffness matrix $\boldsymbol{K}$ is obtained by the assembly of the elemental matrices $\boldsymbol{K}_e(x_e)$.

As in many structural optimization problems where the objective function is not an explicit function of the design variables, the problem stated in (2.73) can be solved by generating a sequence of subproblems that are explicit convex approximations of (2.73) [23].

To obtain such approximation of (2.73) and, therefore, a solution for it, the MMA [36] is here used. This method is a first order algorithm, since it requires information on the values of the objective and constraint functions, as well as on the values of their first derivative with respect to the design variables. Such derivatives, also called *sensitivities*, can be obtained analytically as follows.

The derivative of the compliance with respect to x_e is

$$\frac{\partial c(\mathbf{x})}{\partial x_e} = \boldsymbol{F}^T\frac{\partial \boldsymbol{U}(\mathbf{x})}{\partial x_e} = \boldsymbol{U}(\mathbf{x})^T\boldsymbol{K}(\mathbf{x})\frac{\partial \boldsymbol{U}(\mathbf{x})}{\partial x_e}, \tag{2.78}$$

where the derivative of the displacement vector can be obtained by the differentiation with respect to x_e of the equilibrium equation, which yields

$$\frac{\partial \boldsymbol{U}(\mathbf{x})}{\partial x_e} = -\boldsymbol{K}(\mathbf{x})^{-1}\frac{\partial \boldsymbol{K}(\mathbf{x})}{\partial x_e}\boldsymbol{U}(\mathbf{x}). \tag{2.79}$$

As for the derivative of the stiffness matrix, using equation (2.77),

$$\frac{\partial \boldsymbol{K}(\mathbf{x})}{\partial x_e} = px_e^{p-1}(E_1 - E_0)\boldsymbol{K}_{0e}. \tag{2.80}$$

From equations (2.78), (2.79) and (2.80), and recalling that $\boldsymbol{K}_{0e}$ is an elemental matrix, the sensitivity

of the compliance can be given on element level by

$$\frac{\partial c(\mathbf{x})}{\partial x_e} = -px_e^{p-1}(E_1 - E_0)\boldsymbol{u}_e(\mathbf{x})^T \boldsymbol{K}_{0e}\boldsymbol{u}_e(\mathbf{x}). \tag{2.81}$$

The derivative of the volume constraint function with respect to x_e, $g(\mathbf{x}) = \frac{V(\mathbf{x})}{V_0} - f'$ is, when all finite elements are equal,

$$\frac{\partial g(\mathbf{x})}{\partial x_e} = \frac{1}{n}, \tag{2.82}$$

where n denotes the number of elements used to discretize the design domain.

Note: The formulation here laid out assumes that all elements in the design domain are active, meaning that all of them are part of the domain which can be subjected to changes in the material distribution during the optimization process. For formulations including passive elements, either solid or void elements, see, for instance [37].

Filtering techniques

Topology optimization schemes to the design of optimal structures come typically with numerical instabilities, such as mesh-dependency, local minima and checkerboard patterns [19]. To overcome these issues and to ensure the existence of solutions, a wide number of filtering/regularization techniques has been proposed and is well described in the literature (see, for instance, [34]).

A common approach, and the one used in this work, is the application of a filter to the density field. The filtered densities $\tilde{x}_e$ can be obtained by [38], [39]

$$\tilde{x}_e = \frac{1}{\sum_{i \in N_e} H_{ei} v_i} \sum_{i \in N_e} H_{ei} v_i x_i, \tag{2.83}$$

where N_e is the set of elements i for which the center-to-center distance $\Delta(e,i)$ to element e is smaller than the filter radius r_{min}, H_{ei} is a weight factor defined by $H_{ei} = max(0, \Delta(e,i))$ and v_i is the volume of element i.

When using this approach, the filtered densities $\tilde{x}_e$ are usually referred to as the physical densities, since these are now the ones used in the SIMP curve and therefore in the equilibrium equation and in the objective and volume constraint functions. The densities (design variables) should then be considered as "intermediate mathematical values" and, when showing the optimized results, one should always use the physical density field $\tilde{x}_e$ [34].

Furthermore, the application of this regularization requires the modification of the sensitivities by means of the chain rule [35],

$$\frac{\partial \theta}{\partial x_j} = \sum_{e \in N_j} \frac{\partial \theta}{\partial \tilde{x}_e} \frac{\partial \tilde{x}_e}{\partial x_j} = \sum_{e \in N_j} \frac{1}{\sum_{i \in N_e} H_{ei} v_i} H_{ej} v_j \frac{\partial \theta}{\partial \tilde{x}_e}, \tag{2.84}$$

where θ represents either the compliance c or the volume constraint function g and $\frac{\partial \theta}{\partial \tilde{x}_e}$ is, depending on the sensitivity, still given by equation (2.81) or equation (2.82), replacing only the design variables x_e by

the physical densities $\tilde{x}_e$.

A note on the Method of Moving Asymptotes

The MMA is a nonlinear optimization method developed by Svanberg [36] that has been widely used in the context of topology optimization, since it has proven to work very well even in more demanding structural problems, such as buckling maximization.

When compared to similar methods, such as the Sequential Quadratic Programming or the Convex Linearization methods, the MMA presents great advantages, since it is capable of controlling the degree of "conservatism" of the convex approximation. This either makes the optimization process faster or solvable (meaning that the method converges to a solution). This is accomplished by the so called moving asymptotes that are allowed to change during the optimization process, based on a heuristic approach.

For further details, a comprehensive mathematical description of the method can be found in [36].

2.3.2 Topology optimization for maximization of buckling strength

Buckling can be taken into account when generating optimal structures either by introducing a lower bound on the critical load factor (which means that buckling is in this case addressed as a constraint) or by considering it in the objective function, meaning that the optimized structure is expected to be the best one in terms of buckling strength.

Here, buckling is introduced in the context of topology optimization in the second way mentioned above. The problem, can then be stated as the on of finding the material distribution that maximizes the structure's buckling strength.

The buckling strength of a body is measured by its critical buckling factor, which causes the vanishing of the classical stiffness by geometric stiffness (i.e. the greater this load factor, the greater the buckling strength) and the maximization of it is equivalent to the minimization of the inverse of the critical load factor.

Mathematically, considering a constraint on the material volume and recalling the inherent equilibrium equations, the problem can be formulated as follows [14].

$$
\begin{aligned}
\text{find}: \quad & \mathbf{x} && \text{(design variables)} \\
\text{minimize}: \quad & \frac{1}{\lambda_{cr}} && \text{(objective function)} \\
\text{subject to}: \quad & \boldsymbol{g}(\mathbf{x}) = \frac{V(\mathbf{x})}{V_0} - f' \leq 0 && \text{(constraint function - volume)} \\
& \boldsymbol{K}(\mathbf{x})\boldsymbol{U}(\mathbf{x}) = \boldsymbol{F} && \text{(constraint function - fundamental equilibrium equation)} \\
& (\boldsymbol{K}(\mathbf{x}) + \lambda_{cr}\boldsymbol{G}(\mathbf{x}, \boldsymbol{U}(\mathbf{x})))\boldsymbol{\phi} = 0 && \text{(constraint function - secondary equilibrium equation)} \\
& \mathbf{x}_{min} \leq \mathbf{x} \leq \mathbf{1} && \text{(constraint on the design)},
\end{aligned}
\tag{2.85}
$$

where $\boldsymbol{G}$ denotes the geometric stiffness matrix, λ_{cr} the critical buckling load factor and the remaining

quantities are defined as before.

The SIMP material model described in the previous section cannot be used in this case, since it causes the appearance of artificial buckling modes in the low-density regions [40].

To overcome this issue, a method proposed in [24] is here employed. This model uses different interpolations of the Young's modulus for the construction of the elemental stiffness and geometric stiffness matrices,

$$E_k(x_e) = E_0 + x_e^p(E_1 - E_0), \tag{2.86}$$

$$E_\sigma(x_e) = x_e^p E_1, \tag{2.87}$$

where $E_k(x_e)$ and $E_\sigma(x_e)$ are the interpolations used when building the element stiffness matrices and the geometric stiffness matrices, respectively, E_0 can be interpreted as the Young's modulus assigned to void regions and E_1 the one of the solid material. As it can be seen from the equations above, the interpolation for the stiffness matrix corresponds to the modified SIMP approach presented in the previous section.

These interpolations lead to two different constitutive matrices, which can be obtained, for plane stress problems, by equations (2.75) and (2.76), substituting only the modified SIMP curve by the respective interpolation.

From this, the element stiffness and geometric stiffness matrices are given, respectively, by

$$\boldsymbol{K}_e(x_e) = E_k(x_e)\boldsymbol{K}_{0e}, \tag{2.88}$$

$$\boldsymbol{G}_e = E_\sigma(x_e)\boldsymbol{G}_{0e}\left[\boldsymbol{u}_e(x_e)\right], \tag{2.89}$$

where $\boldsymbol{K}_{0e}$ is defined as before and $\boldsymbol{G}_{0e}$ is the geometric stiffness matrix for an element with unitary Young's modulus, which can still be obtained from the equations in Appendix A, provided that the constitutive matrix is the one explained in the previous section.

To obtain suitable expressions for the calculation of the sensitivities, one can use the Rayleigh quotient as an approximation of the buckling load factors [14]. By doing so, the inverse of the critical load factor becomes

$$\frac{1}{\lambda_{cr}} = \max_{\boldsymbol{\phi}\in\mathbb{R}^n, \boldsymbol{\phi}\neq\mathbf{0}} \frac{\boldsymbol{\phi}^T\boldsymbol{G}(\mathbf{x}, \boldsymbol{U}(\mathbf{x})))\boldsymbol{\phi}}{\boldsymbol{\phi}^T\boldsymbol{K}(\mathbf{x})\boldsymbol{\phi}}, \tag{2.90}$$

where n is the total number of eigenvalues, assumed positive and $\lambda_1 = \lambda_{cr} < \lambda_2 < ... < \lambda_n$.

With this in mind, the sensitivity of the objective function is [14]

$$\frac{\partial}{\partial x_e}\left(\frac{1}{\lambda_{cr}}\right) = \boldsymbol{\phi}_{cr}^T\left(\frac{\partial \boldsymbol{G}}{\partial x_e} - \frac{1}{\lambda_{cr}}\frac{\partial \boldsymbol{K}}{\partial x_e}\right)\boldsymbol{\phi}_{cr} - \boldsymbol{V}_{adj}^T\frac{\partial \boldsymbol{K}}{\partial x_e}\boldsymbol{U}, \tag{2.91}$$

where the critical buckling modes are orthonormalized with respect to the stiffness matrix, i.e. $\boldsymbol{\phi}_{cr}^T\boldsymbol{K}\boldsymbol{\phi}_{cr} =$

1, and $\boldsymbol{V}_{adj}$ is the adjoint displacement field, solution of the adjoint system [40]

$$\boldsymbol{K}\boldsymbol{V}_{adj} = \boldsymbol{\phi}_{cr}^T \frac{\partial \boldsymbol{G}}{\partial \boldsymbol{U}} \boldsymbol{\phi}_{cr} = \begin{Bmatrix} \boldsymbol{\phi}_{cr}^T \frac{\partial \boldsymbol{G}}{\partial u_1} \boldsymbol{\phi}_{cr} \\ ... \\ \boldsymbol{\phi}_{cr}^T \frac{\partial \boldsymbol{G}}{\partial u_d} \boldsymbol{\phi}_{cr} \end{Bmatrix}, \tag{2.92}$$

where d is the number of degrees of freedom of the structure. Further details on calculating the adjoint force $\boldsymbol{\phi}_{cr}^T \frac{\partial \boldsymbol{G}}{\partial \boldsymbol{U}} \boldsymbol{\phi}_{cr}$ are presented in Appendix B.

The first term in equation (2.91) is the generalized gradient of the inverse of the critical load as a function of the design variables only [14]. Therefore, the derivative of the geometric stiffness matrix term should be understood as the explicit derivative, not taking into account the fact that this matrix also depends on the displacement field prior to buckling. This is accounted for by the adjoint term, which is obtained from

$$\left(\frac{\partial \boldsymbol{G}}{\partial x_e}\right)_{total} = \left(\frac{\partial \boldsymbol{G}}{\partial x_e}\right)_{explicit} + \frac{\partial \boldsymbol{G}}{\partial \boldsymbol{U}} \frac{\partial \boldsymbol{U}}{\partial x_e} = \left(\frac{\partial \boldsymbol{G}}{\partial x_e}\right)_{explicit} - \boldsymbol{K}^{-1} \frac{\partial \boldsymbol{G}}{\partial \boldsymbol{U}} \frac{\partial \boldsymbol{K}}{\partial x_e} \boldsymbol{U}, \tag{2.93}$$

where equation (2.79) was used. The terms $total$ and $explicit$ are used to stress the fact that $\boldsymbol{G}$ depends implicitly and explicitly on the design variables.

Details on the solution of the of the adjoint system can be found in Appendix B. The remaining quantities in equation (2.91) are obtained in the same way as done in the previous section and are given by

$$\frac{\partial \boldsymbol{K}}{\partial x_e} = p x_e^{p-1} (E_1 - E_0) \boldsymbol{K}_{e0}, \tag{2.94}$$

$$\frac{\partial \boldsymbol{G}}{\partial x_e} = p x_e^{p-1} E_1 \boldsymbol{G}_{e0}. \tag{2.95}$$

As in the compliance minimization problem, the MMA is here referred to as the updating scheme for the design variables as well as the the density filter there presented as a way of overcoming numerical instabilities.

Chapter 3

Methodology and Implementation

In this section, a description of the carried-out methods and its computational implementation is given by brief indication of the sources when the consulted papers are considered enough, or with more detail when their modification or development was not found in the literature.

3.1 Elastic buckling at separated macro- and micro-scale problems and study of equation on simultaneous macro/micro modes

In what follows, and in contrast to the presented in the previous section, the body forces f are not considered, making the external loading to be only applied surface tractions.

3.1.1 Derivation of governing equations

Before the implementation of the equations presented in chapter 2.2 and in a similar way to that shown in [16], the expressions describing the buckling phenomena at macro- and micro-scale levels where derived by means of the Symbolic Toolbox from Matlab and then compared to the ones presented in [16], where Maple scripts were used. The developed scripts are presented Appendix C. For a better understanding, the scripts' names were kept from [16] and the outlined inputs and outputs refer to the equations and results there presented.

3.1.2 Homogenization - obtaining effective material properties

Much of the work done in this dissertation for obtaining the homogenized material properties was based in [41], where a Matlab implementation of the method is given. Here, the unit cell's domain is discretized using four node isoparametric plane elasticity elements Q4.

In this approach, the calculations of the constitutive matrix, stiffness matrix and force vector are carried-out in terms of the Lamé parameters.

According to the indications provided in the referred paper, the code was adapted to calculate the homogenized elastic material properties of a solid in plane strain state and containing one material and

void (e.g. a micro-structure built from a base linear-elastic isotropic material with holes in it). This is done by ignoring the elements representing the holes when solving the system's equations, requiring only that the base material is "connected" and that the void's material parameters are set to zero. The application to plane stress situations is straight-forward, by the modification of only the definition of the first Lamé parameter, as described in [41].

This function, named *homogenize*, was modified for this thesis to have five user specified inputs (instead of the original six, as the angle ϕ is not needed, since only squared or rectangular elements - and therefore unit cells - are here considered). The user may then specify the lengths of the RVE in $x-$ and $y-$directions, the two Lamé parameters for both the materials (which are set to null when referring to void) and the material indicator matrix **x**. The last input is used to discretize the unit cell. By specifying this matrix, the user chooses which elements of the unit cell refer to the base material and which ones refer to void - the user can then choose a wide number of shapes for the unit cell. For a better understanding, the flowchart in figure 3.1 presents the main steps of the computational implementation of the model.

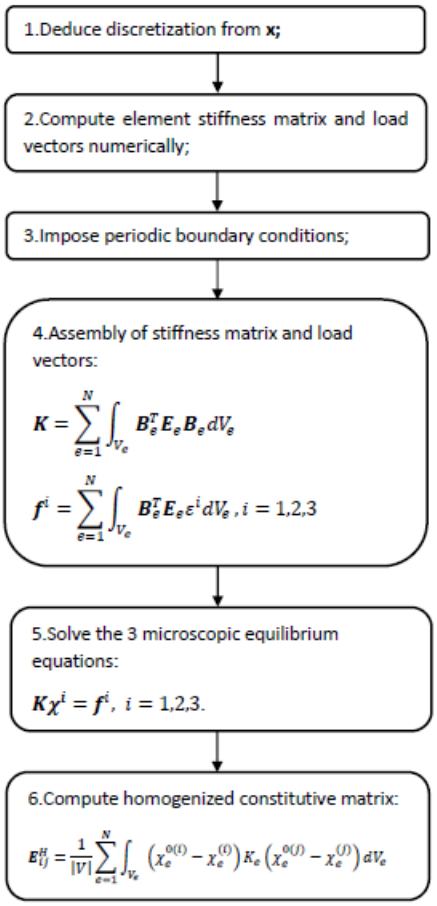

Figure 3.1: Homogenization - a flowchart of its computational implementation.

Furthermore, to make it easier to understand the behavior of the unit cell, some code lines (see Appendix D) that enable the visualization of the RVE's configuration resulting from the characteristic displacements were added to the previous program.

3.1.3 Elastic buckling at macro-scale problems

Recalling section 2, to obtain the macroscopic buckling response it is necessary to calculate the stress resulting from the macroscopic strain field at the fundamental equilibrium state, for which the calculation of the unit cell's homogenized material properties is required.

The eigenvalue problem to be solved for the critical load factor (either at macro-scale or micro-scale cases) requires the calculation of both the stiffness and the geometric stiffness matrices. These matrices, apart from the used element type, are built in the same way for micro- and macroscopic cases - they involve products of components of the stress field existing on the structure prior to buckling and derivatives of the instability modes with respect to the spatial variables.

It can then be understood that the difference in building these matrices for different scale problems resides only in the calculation of the referred stress tensor. So, and as way of obtaining a correct implementation of the geometric stiffness matrix, the Matlab function *Macro_nm* was developed to calculate the critical load for a structure built from a homogeneous solid, that is, no microscopic unit cell periodicity was included in this model. This model was tested and its results were compared with the classical (and analytical) Euler stability theory results.

To treat the macroscopic instability problem for solids with periodic micro-structure, the code for obtaining the effective material properties discussed in the previous section was extended. This function, *Macro_ms*, has nine user inputs: the same five inputs from the *homogenize* function plus the lengths of the macro-structure in both $x-$ and $y-$ directions and the number of macroscopic elements along $x-$ and $y-$ directions that the function uses to discretize the structure. The calculations are also performed for Q4 isoparametric plane elasticity elements using plane stress to express the material elastic properties. The sequence of operations shown in figure 3.2 is carried-out within the developed program.

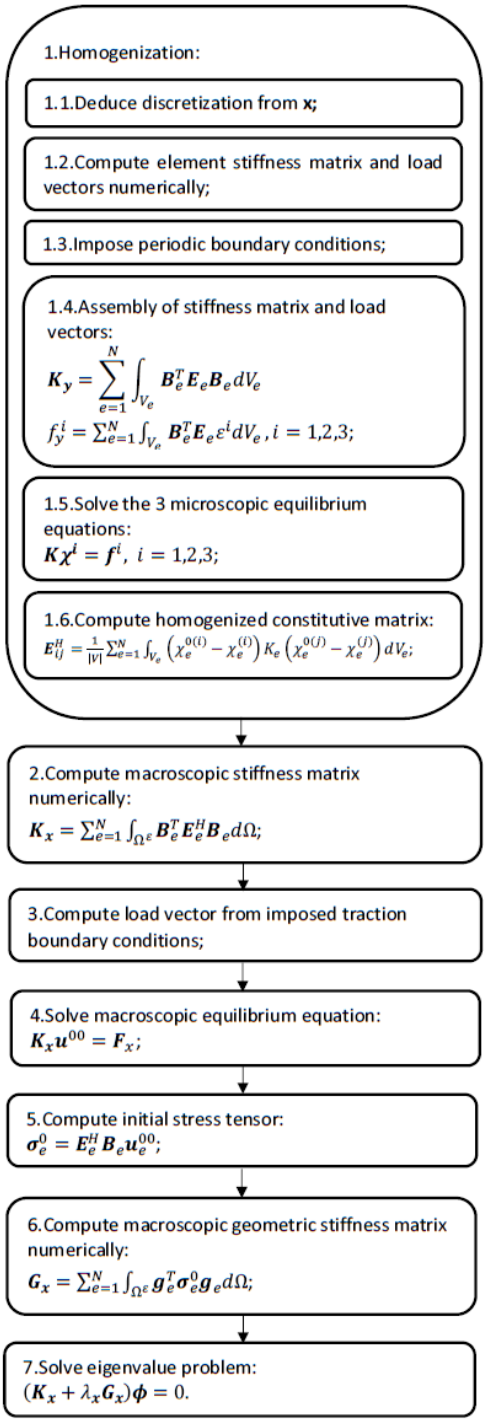

Figure 3.2: Macroscopic instability problem - a flowchart of its computational implementation.

3.1.4 Elastic buckling at micro-scale problems

As mentioned in chapter 2, to address the micro-scale buckling problem, one must first solve the static-elastic problems at the microscopic level. From it, the characteristic displacements of the unit cell, resulting from the imposition of some macroscopic strain field, are obtained, which are then used to compute the microscopic stress field, enabling the construction of the geometric stiffness matrix.

With this in mind, the Matlab function *micro-buckles* was developed, where the computational implementation of the homogenization theory discussed above was used to obtain the referred characteristic displacements. This function, has the same inputs as *homogenize* and performs the calculations using also Q4 plane elasticity elements and plane stress to express the constitutive matrix.

The stiffness matrix used to solve the eigenvalue problem is the same as the one used to solve the static-elastic problem and, therefore, there is is only the need to further implement the geometric stiffness matrix according to Appendix A.

In the same fashion as before, the flowchart in figure 3.3 enables a better understanding of how the computational implementation of the micro-scale instability problem was performed.

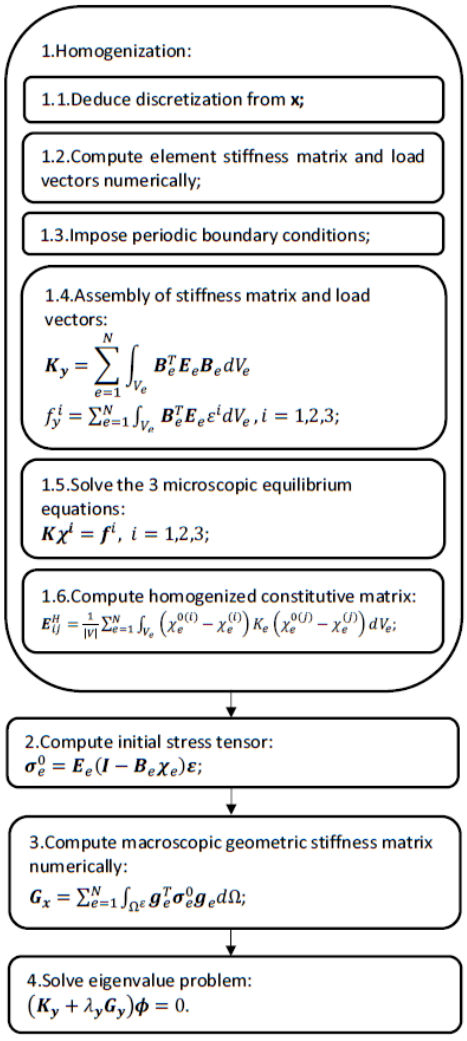

Figure 3.3: Microscopic instability problem - a flowchart of its computational implementation.

3.1.5 Simultaneous macro/micro elastic buckling

To implement the coupled instability problem, equation (2.63) must first be studied.

Recalling that the static solution $\boldsymbol{u}^{00} = \lambda \boldsymbol{u}$, $\boldsymbol{u}^{10} = c^{te}\boldsymbol{\phi}$ and $\boldsymbol{v}^{10} = c^{te}\boldsymbol{\psi}$, equation (2.63) can be rewritten as

$$\int_{\Omega^\varepsilon} \left[E_{ijkm} \left(\frac{\partial \phi_i}{\partial y_j} \frac{\partial \psi_k}{\partial x_m} \right) + E_{ijkm} \left(\frac{\partial \phi_i}{\partial x_j} \frac{\partial \psi_k}{\partial y_m} \right) \right] d\Omega + \lambda_{xy} \int_{\Omega^\varepsilon} \left[\sigma^0_{km} \left(\frac{\partial \phi_c}{\partial y_m} \frac{\partial \psi_c}{\partial x_k} \right) + \sigma^0_{km} \left(\frac{\partial \phi_c}{\partial x_k} \frac{\partial \psi_c}{\partial y_m} \right) \right] d\Omega = 0, \tag{3.1}$$

where

$$\sigma^0_{ij} = \left(E_{ijkm} - E_{ijpq} \frac{\partial \chi^{km}_p}{\partial y_q} \right) \frac{\partial u_i}{\partial x_j} \tag{3.2}$$

and λ_{xy} denotes the coupled instability load factor. The mode ϕ is the solution of the eigenvalue problem and ψ is the test function.

Expanding each term inside the integrals in equation (3.1) and writing them in matrix notation yields

$$E_{ijkm} \left(\frac{\partial \phi_i}{\partial y_j} \frac{\partial \psi_k}{\partial x_m} \right) = \begin{bmatrix} \frac{\partial \psi_1}{\partial x_1} & \frac{\partial \psi_2}{\partial x_2} & \frac{\partial \psi_1}{\partial x_2} + \frac{\partial \psi_2}{\partial x_1} \end{bmatrix} \begin{bmatrix} E_{1111} & E_{1122} & E_{1112} \\ E_{2211} & E_{2222} & E_{2212} \\ E_{1211} & E_{1222} & E_{1212} \end{bmatrix} \begin{bmatrix} \frac{\partial \phi_1}{\partial y_1} \\ \frac{\partial \phi_2}{\partial y_2} \\ \frac{\partial \phi_1}{\partial y_2} + \frac{\partial \phi_2}{\partial y_1} \end{bmatrix} \tag{3.3}$$

$$E_{ijkm} \left(\frac{\partial \phi_i}{\partial x_j} \frac{\partial \psi_k}{\partial y_m} \right) = \begin{bmatrix} \frac{\partial \psi_1}{\partial y_1} & \frac{\partial \psi_2}{\partial y_2} & \frac{\partial \psi_1}{\partial y_2} + \frac{\partial \psi_2}{\partial y_1} \end{bmatrix} \begin{bmatrix} E_{1111} & E_{1122} & E_{1112} \\ E_{2211} & E_{2222} & E_{2212} \\ E_{1211} & E_{1222} & E_{1212} \end{bmatrix} \begin{bmatrix} \frac{\partial \phi_1}{\partial x_1} \\ \frac{\partial \phi_2}{\partial x_2} \\ \frac{\partial \phi_1}{\partial x_2} + \frac{\partial \phi_2}{\partial x_1} \end{bmatrix} \tag{3.4}$$

$$\sigma^0_{km} \left(\frac{\partial \phi_c}{\partial y_m} \frac{\partial \psi_c}{\partial x_k} \right) = \begin{bmatrix} \frac{\partial \psi_1}{\partial x_1} & \frac{\partial \psi_1}{\partial x_2} & \frac{\partial \psi_2}{\partial x_1} & \frac{\partial \psi_2}{\partial x_2} \end{bmatrix} \begin{bmatrix} \sigma_{11} & \sigma_{12} & 0 & 0 \\ \sigma_{12} & \sigma_{22} & 0 & 0 \\ 0 & 0 & \sigma_{11} & \sigma_{12} \\ 0 & 0 & \sigma_{12} & \sigma_{22} \end{bmatrix} \begin{bmatrix} \frac{\partial \phi_1}{\partial y_1} \\ \frac{\partial \phi_1}{\partial y_2} \\ \frac{\partial \phi_2}{\partial y_1} \\ \frac{\partial \phi_2}{\partial y_2} \end{bmatrix} \tag{3.5}$$

$$\sigma^0_{km} \left(\frac{\partial \phi_c}{\partial x_k} \frac{\partial \psi_c}{\partial y_m} \right) = \begin{bmatrix} \frac{\partial \psi_1}{\partial y_1} & \frac{\partial \psi_1}{\partial y_2} & \frac{\partial \psi_2}{\partial y_1} & \frac{\partial \psi_2}{\partial y_2} \end{bmatrix} \begin{bmatrix} \sigma_{11} & \sigma_{12} & 0 & 0 \\ \sigma_{12} & \sigma_{22} & 0 & 0 \\ 0 & 0 & \sigma_{11} & \sigma_{12} \\ 0 & 0 & \sigma_{12} & \sigma_{22} \end{bmatrix} \begin{bmatrix} \frac{\partial \phi_1}{\partial x_1} \\ \frac{\partial \phi_1}{\partial x_2} \\ \frac{\partial \phi_2}{\partial x_1} \\ \frac{\partial \phi_2}{\partial x_2} \end{bmatrix} \tag{3.6}$$

Given a double discretization of the model (one at the macro-scale and another at the micro-scale levels) and since in equation (3.1) the integrations are performed in the macroscopic domain, the resultant global matrices can be obtained by the assemblage of macro-elemental corresponding ones. Furthermore, a macroscopic element can be seen as a domain discretized by microscopic elements. Following this line of thought, the global matrices can be obtained by individual assemblies of microscopic matrices corresponding to micro-elements within a macro-element followed by the assembly of the obtained macroscopic matrices. Mathematically, for a given macro-scale element E, the integrals in equation (3.1) become, by the some order they appear in equation (3.1),

$$\int_{\Omega^E} \sum_{e=1}^{n} \left[\int_{Y^e} E_{ijkm} \left(\frac{\partial \phi_i}{\partial y_j} \frac{\partial \psi_k}{\partial x_m} \right) dY + \int_{Y^e} E_{ijkm} \left(\frac{\partial \phi_i}{\partial x_j} \frac{\partial \psi_k}{\partial y_m} \right) dY \right] d\Omega \text{ and} \tag{3.7}$$

$$\int_{\Omega^E} \sum_{e=1}^{n} \left[\int_{Y^e} \sigma^0_{km} \left(\frac{\partial \phi_c}{\partial y_m} \frac{\partial \psi_c}{\partial x_k} \right) dY + \int_{Y^e} \sigma^0_{km} \left(\frac{\partial \phi_c}{\partial x_k} \frac{\partial \psi_c}{\partial y_m} \right) dY \right] d\Omega, \tag{3.8}$$

where n refers to the number of microscopic elements present in a macroscopic element. The summation has the meaning of a finite element assembly operation (to obtain a macro-elemental matrix).

If elements of the same type (including same number of nodes and shape) are used for macro- and micro-scales and if the discretization is the same at both levels, then the nodes of macro- and micro-elements will be the same and the assembly operations within each macro-scale element drop out.

From a double discretization of the model, the instability modes are then given by the interpolation of their nodal values:

$$\phi_1(x_1, y_1) \approx \sum_{I=1}^{NN} \phi_1^I N_x^I + \sum_{i=1}^{nn} \phi_1^i N_y^i, \ \phi_2(x_2, y_2) \approx \sum_{J=1}^{NN} \phi_2^J N_x^J + \sum_{j=1}^{nn} \phi_2^j N_y^j, \tag{3.9}$$

$$\psi_1(x_1, y_1) \approx \sum_{I=1}^{NN} \psi_1^I N_x^I + \sum_{i=1}^{nn} \psi_1^i N_y^i, \ \psi_2(x_2, y_2) \approx \sum_{J=1}^{NN} \psi_2^J N_x^J + \sum_{j=1}^{nn} \psi_2^j N_y^j, \tag{3.10}$$

where NN denotes the number of nodal points per macroscopic element, nn the number of nodes per microscopic element and N_x and N_y the shape functions for a macro-element and for a micro-element, respectively. ϕ_1^I and ϕ_2^J are the nodal modes of a macro-scale element in directions 1 and 2, respectively, and ϕ_1^i and ϕ_2^j the nodal modes of a micro-scale element in directions 1 and 2.

It should be noted that, in the given approximations, the exact ratio between each sum of the product of nodal modes and shape functions is irrelevant, since all terms in equation (3.1) involve the product between two derivatives, one of each scale.

By the application of these approximations,

$$\begin{bmatrix} \frac{\partial \phi_1}{\partial x_1} \\ \frac{\partial \phi_2}{\partial x_2} \\ \frac{\partial \phi_1}{\partial x_2} + \frac{\partial \phi_2}{\partial x_1} \end{bmatrix} = \begin{bmatrix} \frac{\partial N_x^1}{\partial x_1} & 0 & \dots & \frac{\partial N_x^{NN}}{\partial x_1} & 0 \\ 0 & \frac{\partial N_x^1}{\partial x_2} & \dots & 0 & \frac{\partial N_x^{NN}}{\partial x_2} \\ \frac{\partial N_x^1}{\partial x_2} & \frac{\partial N_x^1}{\partial x_1} & \dots & \frac{\partial N_x^{NN}}{\partial x_2} & \frac{\partial N_x^{NN}}{\partial x_1} \end{bmatrix} \begin{bmatrix} \phi_1^1 \\ \phi_2^1 \\ \dots \\ \phi_1^{NN} \\ \phi_2^{NN} \end{bmatrix} = \boldsymbol{B_x} \boldsymbol{\phi_x}, \tag{3.11}$$

$$\begin{bmatrix} \frac{\partial \phi_1}{\partial y_1} \\ \frac{\partial \phi_1}{\partial y_2} \\ \frac{\partial \phi_2}{\partial y_1} \\ \frac{\partial \phi_2}{\partial y_2} \end{bmatrix} = \begin{bmatrix} \frac{\partial N_y^1}{\partial y_1} & 0 & \dots & \frac{\partial N_y^{nn}}{\partial y_1} & 0 \\ \frac{\partial N_y^1}{\partial y_2} & 0 & \dots & \frac{\partial N_y^{nn}}{\partial y_2} & 0 \\ 0 & \frac{\partial N_y^1}{\partial y_1} & \dots & 0 & \frac{\partial N_y^{nn}}{\partial y_1} \\ 0 & \frac{\partial N_y^1}{\partial y_2} & \dots & 0 & \frac{\partial N_y^{nn}}{\partial y_2} \end{bmatrix} \begin{bmatrix} \phi_1^1 \\ \phi_2^1 \\ \dots \\ \phi_1^{nn} \\ \phi_2^{nn} \end{bmatrix} \boldsymbol{g_y} \boldsymbol{\phi_y}, \tag{3.12}$$

and the same goes for the other derivative vectors in equations (3.3), (3.4), (3.5) and (3.6).

Furthermore, since the discretization is the same at both scale-levels, the introduction of the approx-

imations (3.9) and (3.10) yields $\boldsymbol{N_x} = \boldsymbol{N_y}$, $\boldsymbol{B_x} = \boldsymbol{B_y}$, $\boldsymbol{g_x} = \boldsymbol{g_y}$, $\boldsymbol{\phi_x} = \boldsymbol{\phi_y}$ and $\boldsymbol{\psi_x} = \boldsymbol{\psi_y}$, which, as suggested by [16], results in the following system of equations

$$(\boldsymbol{K_{xy}} + \lambda_{xy}\boldsymbol{G_{xy}})\,\boldsymbol{\phi} = 0. \tag{3.13}$$

The global coupled stiffness matrix, $\boldsymbol{K_{xy}}$, is obtained by the assembly of the corresponding elemental ones given by

$$\boldsymbol{K^E_{xy}} = \int_{\Omega^E}\int_{Y^e}\left[\boldsymbol{B}_E^T\boldsymbol{E}_e\boldsymbol{B}_e + \boldsymbol{B}_e^T\boldsymbol{E}_e\boldsymbol{B}_E\right]dY\,d\Omega \tag{3.14}$$

and the global coupled geometric stiffness matrix,$\boldsymbol{G_{xy}}$, by the assembly of

$$\boldsymbol{G^E_{xy}} = \int_{\Omega^E}\int_{Y^e}\left[\boldsymbol{g}_E^T{\boldsymbol{\sigma^0}}_e\boldsymbol{g}_e + \boldsymbol{g}_e^T{\boldsymbol{\sigma^0}}_e\boldsymbol{g}_E\right]dY\,d\Omega, \tag{3.15}$$

where e refers to a micro-scale element and $\boldsymbol{\sigma^0}$ is defined in Appendix A.

Applying numerical integration to evaluate the integrals by means of the Gauss quadrature rule yields

$$\boldsymbol{K^E_{xy}} = \sum_{a=1}^{NPG1}\sum_{b=1}^{NPG2}\left[\sum_{c=1}^{npg1}\sum_{d=1}^{npg2}\left(\boldsymbol{B}_E^T\boldsymbol{E}_e\boldsymbol{B}_e + \boldsymbol{B}_e^T\boldsymbol{E}_e\boldsymbol{B}_E\right)det\boldsymbol{J}_y w_d w_c\right]det\boldsymbol{J}_x w_b w_a \text{ and} \tag{3.16}$$

$$\boldsymbol{G^E_{xy}} = \sum_{a=1}^{NPG1}\sum_{b=1}^{NPG2}\left[\sum_{c=1}^{npg1}\sum_{d=1}^{npg2}\left(\boldsymbol{g}_E^T{\boldsymbol{\sigma^0}}_e\boldsymbol{g}_e + \boldsymbol{g}_e^T{\boldsymbol{\sigma^0}}_e\boldsymbol{g}_E\right)det\boldsymbol{J}_y w_d w_c\right]det\boldsymbol{J}_x w_b w_a, \tag{3.17}$$

where $NPG1$ and $NPG2$ refers to the number of Gauss points in both directions for the macroscopic elements, $npg1$ and $npg2$ to the number of Gauss points for the microscopic elements, w_i the weight factor for the respective Gauss point and $det\boldsymbol{J_i}$ the determinant of the Jacobian matrix related with the element mapping with a master element. It should be, again, noted that $\boldsymbol{B}_E$ and $\boldsymbol{B}_e$ are the same matrices, since the shape functions for both scales are the same as a result of choosing the same discretization for both domains.

The application of the same discretization for both domains will, of course, generate an "excessively refined" mesh for the macroscopic domain. However, it does not make the solution any worse (if anything, only better, as it is known from the convergence of the finite element method) and it is assumed that it does not make the two domains the same - $\boldsymbol{y} \approx \frac{\boldsymbol{x}}{\varepsilon}$ still holds.

Moreover, it should be noted that for the construction of the geometric stiffness matrix, the calculation of the initial stress components is required. For it, the macroscopic static-elastic equations must be solved for the fundamental equilibrium position for which, as discussed before, the homogenized material properties must be obtained. Recalling previous sections, to perform the homogenization of the unit cell, the characteristic displacements, solution of the static-elastic problems at the micro-scale level, must be found. This means that, before addressing the coupled instability problem, it is necessary to, by this order:

- Solve the static-elastic problems at the micro-scale level;
- Calculate the homogenized material properties;

- Solve the static-elastic problem at the macro-scale level.

The proposed computational implementation makes use of the previous considerations and has seven user specified inputs: the lengths in $x-$ and $y-$ directions of the structure, the lengths in $x-$ and $y-$ directions of the unit cell, the two Lamé parameters (each of them has two entries: one for the base material and one for void; when referred to void these parameters should be set to zero) and the material indicator matrix **x**, which works in the same way has in the *homogenize* function. As in the case of the homogenization computational model, **x** is used to discretize the RVE and, by means of the ratios between the lengths in each direction of the unit cell and the structure, the macroscopic discretization is deduced, so that both discretizations are the same in both domains.

Here, and as in the previous implementations, Q4 plane elasticity elements are used and the material constitutive relations are expressed by the plane stress equations. The steps in figure 3.4 are carried out in the developed Matlab function *Coupleds*.

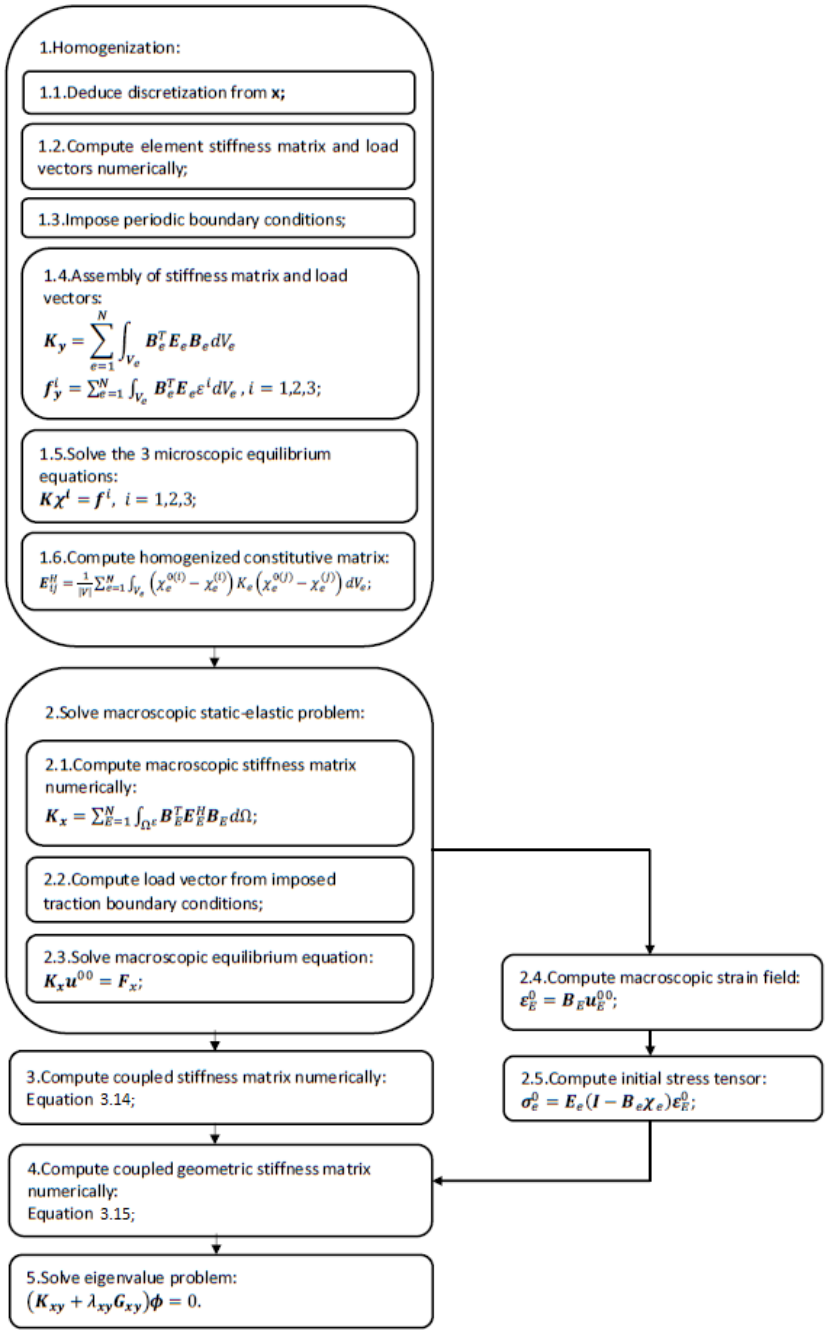

Figure 3.4: Coupled instability problem - a flowchart of its computational implementation.

3.2 Topology optimization – structures built from linear-elastic materials

3.2.1 Compliance minimization problem

Here, the Matlab implementation given in [35] is modified to address the compliance minimization with a volume constraint problem (2.73) using the MMA as an updating scheme for the design variables.

In [35], to solve the optimization problem, a density-based approach is followed, where the modified SIMP curve presented in the previous chapter is used. Furthermore, two filtering techniques are available – sensitivity filter and the density filter described in the previous chapeter. To solve the compliance optimization problem, a "standard" Optimality Criteria method is there used.

This function, named *top88* [35] has six user inputs: the number of elements is $x-$ and $y-$direction, the maximum allowed total volume fraction, the value of the penalization factor to be used in the SIMP curve, the filter radius and a parameter *ft* for selecting the desired filtering method (*ft*=1 corresponds to the sensitivity filter and *ft*=2 to the density filter).

To include the MMA algorithm as the solver of the optimization problem and using the MMA Matlab implementation provided by Prof. Svanberg, the recommendations provided in [42] regarding the type of problem to which the MMA is applied to as well as the recommendations in [19] regarding specifically the compliance minimization problem were followed.

Before the iteration process begins, the following code lines were added.

```
%% INITIALIZE MMA OPTIMIZER
 m     = 1;
 n     = nelx*nely;
 xmin  = zeros(n,1);
 xmax  = ones(n,1);
 xold1 = x(:);
 xold2 = x(:);
 low   = ones(n,1);
 upp   = ones(n,1);
 a0    = 1;
 a     = zeros(m,1);
 ccc = 10000*ones(m,1);
 d     = zeros(m,1);
```

Then, the code lines referring to the Optimatity Criteria method were replaced by the following ones.

```
%% METHOD OF MOVING ASYMPTOTES
 xval  = x(:);
 f0val = c;
 df0dx = dc(:);
 fval  = sum(xPhys(:))/(volfrac*nelx*nely) - 1;
 dfdx  = dv(:)' / (volfrac*nelx*nely);
 [xmma, ~, ~, ~, ~, ~, ~, ~, ~, low,upp] = ...
 mmasub(m, n, loop, xval, xmin, xmax, xold1, xold2, ...
 f0val,df0dx,fval,dfdx,low,upp,a0,a,ccc,d);
 % Update MMA Variables
 xnew     = reshape(xmma,nely,nelx);
 xPhys(:) = (H*xnew(:))./Hs;
 xold2    = xold1(:);
 xold1    = x(:);
 change = max(abs(xnew(:)-x(:)));
 x = xnew;
```

The remaining code lines of the original implementation from [35] were kept and the resultant Matlab function was tested for some benchmark examples.

3.2.2 Buckling strength maximization problem

To address the topology optimization for maximum buckling strength of structures problem, a Matlab function, named *TopOptBuckling*, was developed, based on the previous implementation of the compliance minimization problem. Here, as already mentioned, the calculations are performed only for simple eigenvalues (no multiplicity of eigenvalues is considered).

This function has eight user inputs: the lengths of the structure in the $x-$ and $y-$directions, the number of elements along the $x-$ and $y-$directions, the maximum allowed total volume fraction, the value of penalization factor, the filter radius and the tolerance value used to end the optimization process.

Furthermore, the proposed numerical implementation uses Q4 isoparametric plane elasticity elements and the material properties are expressed by means of the plane stress equations.

For a better understanding of the implementation itself, all the finite element calculations, which include the computation of the stiffness matrix and the geometric stiffness matrix, the solution of the equilibrium equations, and the majority of the quantities required for the calculation of the sensitivities, were performed by means of the developed Matlab function *FE_analysis* and then returned to the main function *TopOptBuckling*. The flowchart in figure 3.5 provides a better insight into the developed computational model.

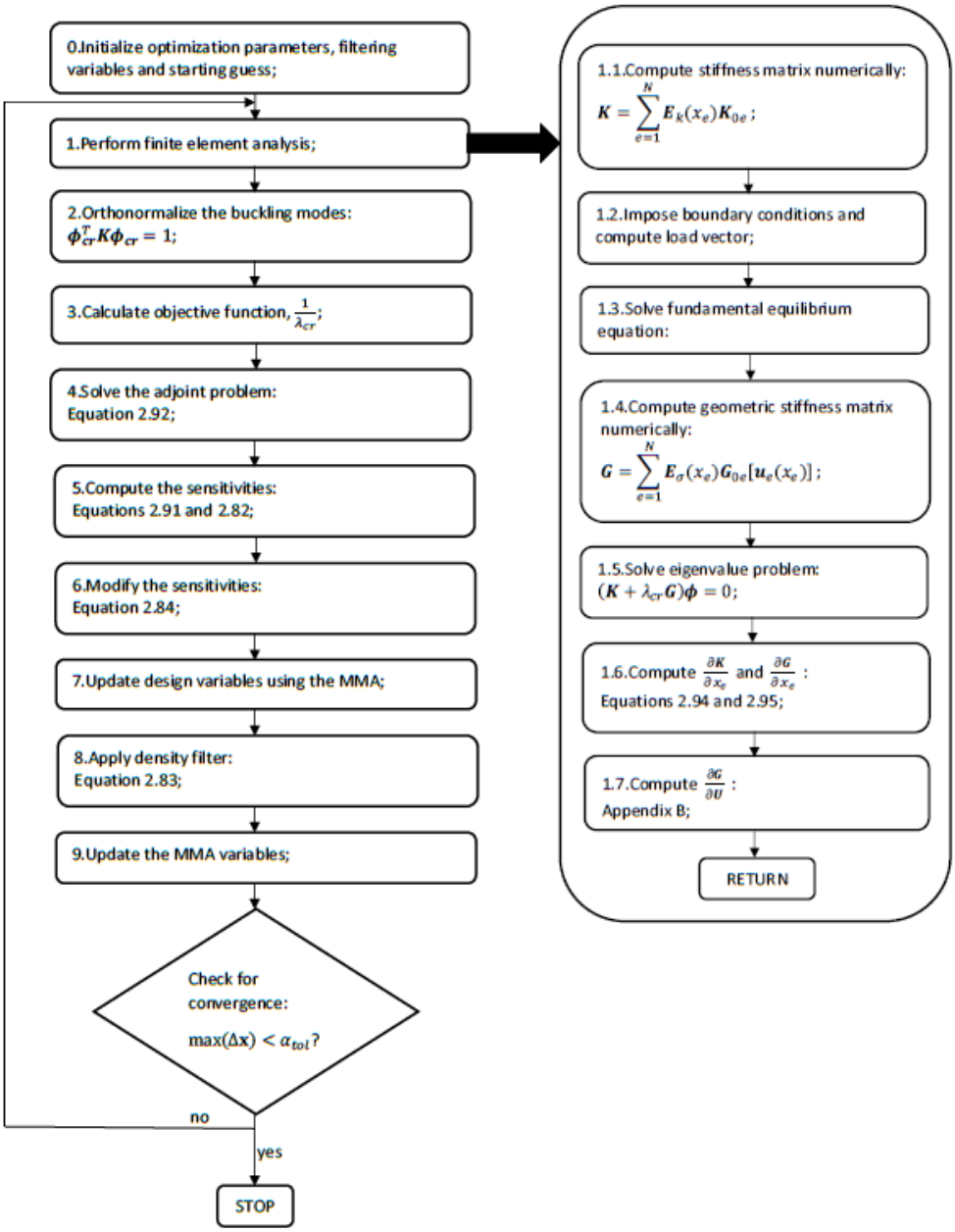

Figure 3.5: Topology optimization for maximum buckling strength - a flowchart of its computational implementation.

Chapter 4

Results

In this section, the most meaningful results are summarized, together with the respective problems descriptions. Verification examples are used to apply the developed or analysed model implementations, whenever such operations are possible. With that in mind, some problems found in the literature are reproduced using the developed computational models and the results of both analysis are compared. When such problems are not found and when considered necessary, test cases to verify the numerical implementations are elaborated. Some comments regarding the obtained solutions are also made.

4.1 Homogenized material properties

Although the numerical implementation of the homogenization theory was purely based on the one presented in [41] (only an extension to enable the visualization of the deformed shape of the unit cell was here made), an example found in [43] was reproduced using the extended *homogenize* function and plotted against the results there presented.

From [43], the example regarding a square unit cell with a rectangular hole was addressed. Here, only the initial mesh was reproduced. This mesh discretizes the unit cell in 20x20 four node isoparametric elements for plane elasticity. The base material's constitutive relations are expressed using the plane stress relations, where $E_{11} = E_{22} = 30$ and $E_{12} = E_{66} = 10$. The RVE side has a unitary length and the hole's dimensions are 0.6 and 0.4 (all quantities used are assumed to have consistent units). The undeformed configuration and the deformed configurations of the unit cell resulting from each of the applied independent unit strain fields and given by *homogenize* can be seen in figure 4.1. A comparison between the results of the components of the homogenized elasticity tensor given by [43] and *homogenize* is shown in table 4.1.

Table 4.1: Homogenized elastic properties - results comparison from [43] and *homogenize*.

Results	E^H_{11}	E^H_{12}	E^H_{22}	E^H_{66}
From [43]	13.015	3.241	17.552	2.785
From *homogenize*	13.015	3.241	17.552	2.785

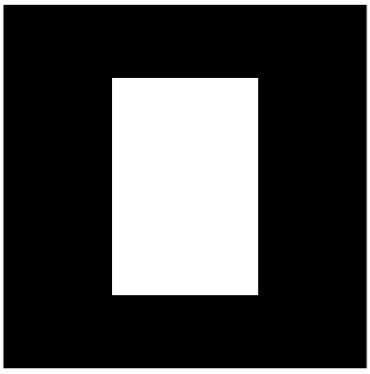

(a) Undeformed shape

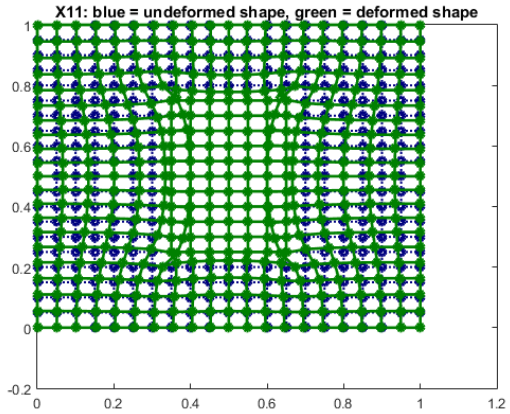

(b) Deformed shape from the application of a unit strain field in $x-$ direction

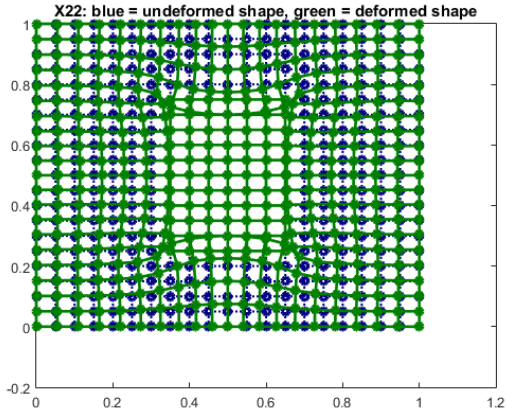

(c) Deformed shape from the application of a unit strain field in $y-$ direction

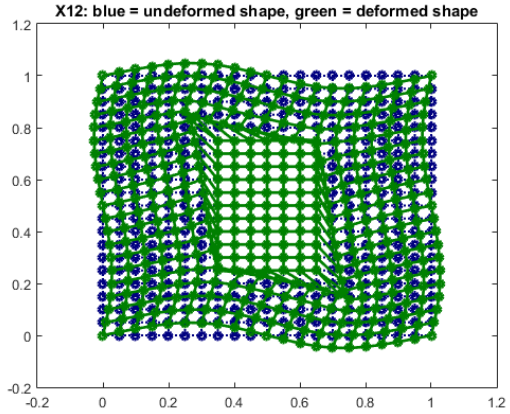

(d) Deformed shape from the application of a unit shear strain field in $xy-$ plane

Figure 4.1: Squared cell with a rectangular hole: undeformed vs. deformed shapes corresponding to the application of three independent unit strains.

As expected, given that the conditions used in [43] were exactly kept when using the *homogenize* function, both results were exactly the same. The deformed shapes also agree with the ones found for squared cells with rectangular holes in the literature (see, for instance, the examples presented in [16]). Therefore, the used implementation given by [41] provides, as expected, accurate results for the homogenized properties of cells built by a base material with holes. Moreover, the developed *homogenize* extension to enable the visualization of the deformed shapes of the RVE was also verified by this example.

4.2 Implementation of the macro-scale geometric stiffness matrix

As mentioned in section 3.1, a numerical model for the calculation of the critical load of a homogeneous body without a periodic micro-structure was made. This enables a much easier verification of the implementation of the geometric stiffness matrix that still applies to the other mentioned buckling cases.

With that in mind, a Matlab function *Macro_nm* was developed to calculate the critical load of a

column to be compared with the known solution given by the *Euler's Column Formula*. Details on this analytical theory for the calculation of buckling loads in beams and frames can be found in [44].

Here, a beam subjected to a compressing axial load is considered. The left end of the beam is constricted in such a way that movements along the beam's direction are not allowed; the right end of the beam is free and a central compressing load is there applied. The mentioned analytical solution for this specific instability case is

$$P_{cr} = \frac{\pi^2 EI}{4L^2}, \tag{4.1}$$

where L denotes the beam's length, E the Young's modulus of the beam's material and I the moment of inertia of the beam's cross-sectional area. Using *Macro_nm*, this structure was discretized using Q4 isoparametric plane elasticity elements for plane stress. The load was applied as a uniform stress distribution of -1MPa in the $x-$ direction at the beams's right end and all nodes referring to the left end were constricted in the $x-$ direction. The modelled beam has a length $L = 40$m, a height $h = 5$m and a thickness $b = 1$m. The material is described by a Young's modulus $E = 2.1$MPa and a Poisson's ratio $\nu = 0.3$.

The body was initially discretized using 16 finite elements and the mesh was progressively refined up to a final value of 800 elements. The convergence history of the analysis with the performed refinement of the mesh can be seen in figure 4.2.

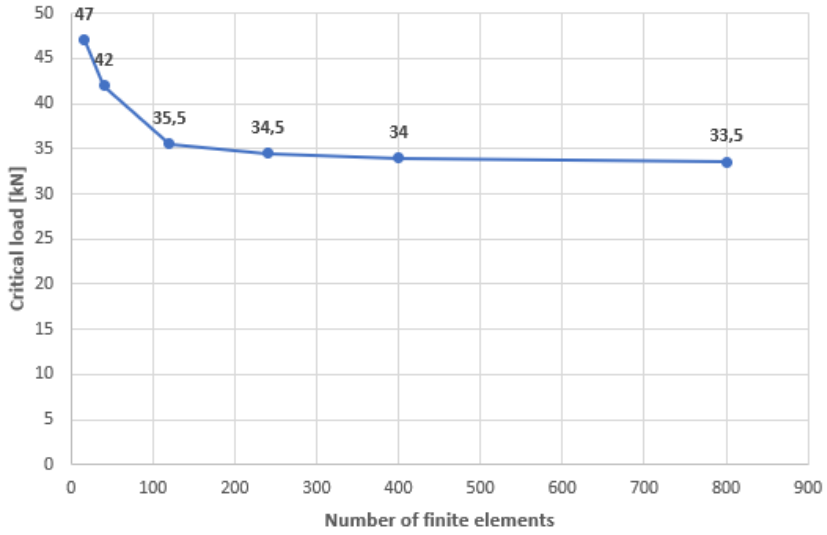

Figure 4.2: Convergence analysis for *Macro_nm* results of the critical load.

Taking the final mesh, the result of *Macro_nm* for the first (critical) and second instability modes are shown in figure 4.3 and a comparison between the critical loads given by the developed function and the *Euler's Comumn Formula* is given in table 4.2.

From table 4.2, it can be seen that as the the mesh is refined, the critical load value from the *Macro_nm* function approaches the analytical value given by the Euler's formula. Furthermore, the presented instability modes in figure 4.3 agree with the ones known from the literature (see, for instance [44]). Thus, the implementation of this particular stability problem and therefore, the implementation of the geometric stiffness matrix, is, to some extent, verified.

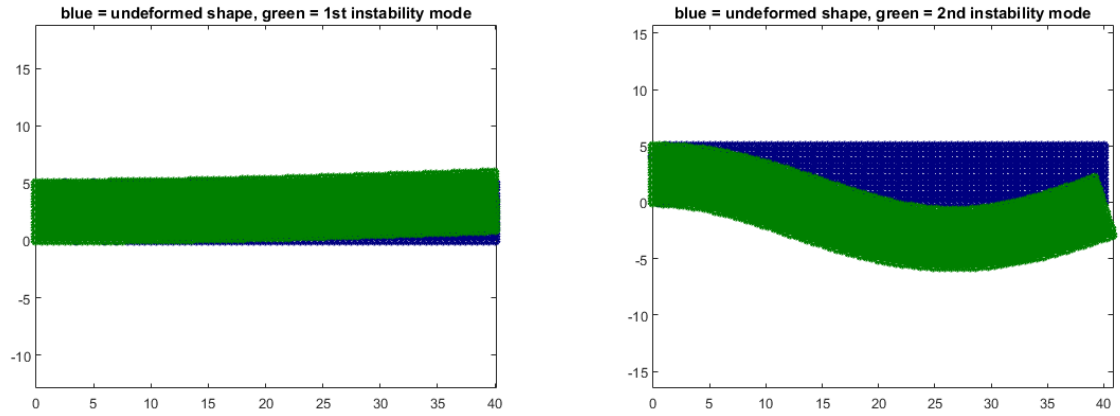

(a) Critical instability mode shape

(b) Second instability mode shape

Figure 4.3: First two macro-scale instability modes: undeformed vs. deformed shapes.

Table 4.2: Comparison of the results from *Macro_nm* and the analytical Euler's formula.

	Macro_nm						Euler's formula (4.1)
Nº finite elements	16	40	120	240	400	800	
Pcr [kN]	47.000	42.000	35.500	34.500	34.000	33.500	33.734
Error [%]	39.325	24.503	5.235	2.271	0.788	0.694	

4.3 Y-Periodic micro-scale critical load for structures built from a solid with periodic micro-structure

Here, example 2 from [12] is presented and reproduced using the *micro_buckles* function. In this example, the authors compare the performance regarding microscopic buckling strength of different unit cells having the same material density and differing only in the material's distribution in the RVE's domain. There, the unit cells are discretized using 10x10 four node isoparametric elements for plane elasticity and are all subjected to the same macroscopic strain field of $\varepsilon^0 = C^{te}\{-1\ 0\ 0\}$. All the conditions used in [12] to perform the comparison between different unit cells can be replicated exactly by *micro_buckles* - same number and type of elements and same material densities and distributions.

The tested material distributions and their critical instability modes obtained with *micro_buckles* can be seen in figures 4.4, 4.5, 4.6, 4.7 and 4.8 and the results for the critical load together with the ones presented in [12] are outlined in table 4.3.

Both the values of the microscopic critical loads and the critical mode shapes were obtained very identically to the ones presented in [12], which enables the validation of the *micro_buckles* function, at least in the presented cases.

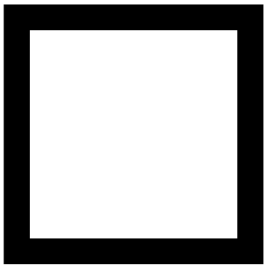

(a) Undeformed shape

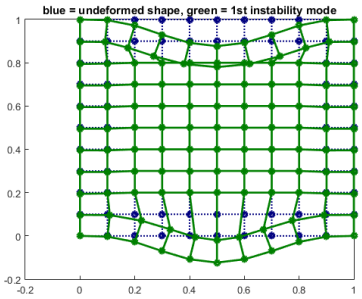

(b) Critical instability mode shape

Figure 4.4: Initial material distribution.

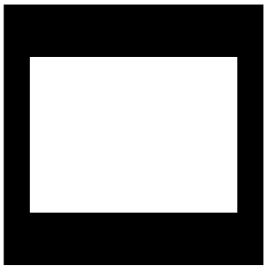

(a) Undeformed shape

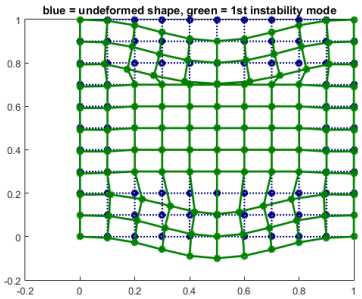

(b) Critical instability mode shape

Figure 4.5: Material distribution 1.

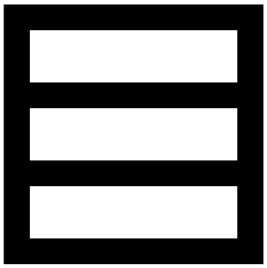

(a) Undeformed shape

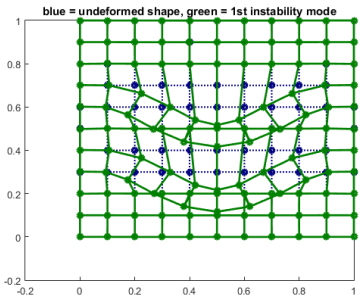

(b) Critical instability mode shape

Figure 4.6: Material distribution 2.

Table 4.3: Results comparison from [12] and *micro_buckles*.

Distribution case	ρ	λ_{cr} from [12]	λ_{cr} from *microbuckles*
Initial	0.3600	0.1170	0.1177
1	0.5200	0.2080	0.2087
2	0.5200	0.0520	0.0528
3	0.5200	0.0000	0.0000
4	0.5200	0.0000	0.0000

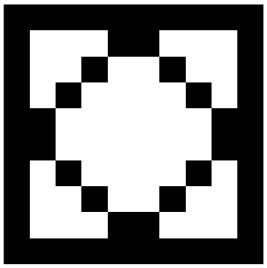

(a) Undeformed shape

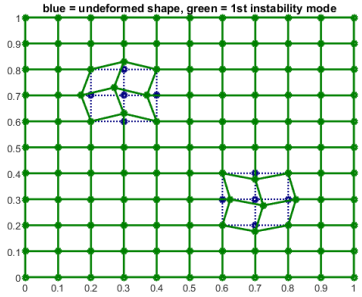

(b) Critical instability mode shape

Figure 4.7: Material distribution 3.

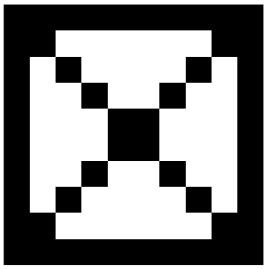

(a) Undeformed shape

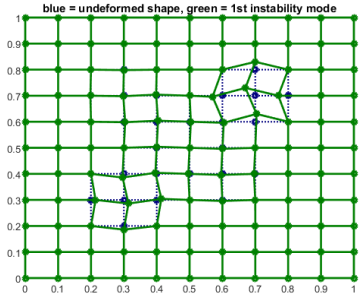

(b) Critical instability mode shape

Figure 4.8: Material distribution 4.

The same conclusions as in [12] can be here drawn - the best material distribution regarding buckling is the material distribution 1, which corresponds to a concentration of the additional material (additional when compared to the initial material distribution) ”at the members aligned with the direction of the non-zero strain component”.

4.4 Macroscopic instability problem – structures built from solids with periodic micro-structure

In this section, the implementation given in 3.1.3 from chapter 3 is applied to the same problem as in 4.2 for a column subjected to a compressing load. Here, the column is built from a solid having a periodic repetition of a micro-structure - a squared cell with a squared hole. The RVE has the same base material as in 4.2, a material density of 0.64 and an exterior side measuring 0.01m. The homogenized material properties are obtained by the discretization of the unit cell in 10x10 finite elements.

The results for the critical load are shown in figure 4.9, where a convergence analysis of the problem is presented. Recalling the results for the same problem where the structure didn’t have a specific micro-structure shown in figure 4.2, it can be seen, that the critical load value decreases more than 50% when a unit cell of this type is considered. This result was expected, since the reduction of material density results in a structure with a lower buckling strength. Furthermore, the obtained critical and second instability modes were, as also expected, identical to those presented in section 4.2.

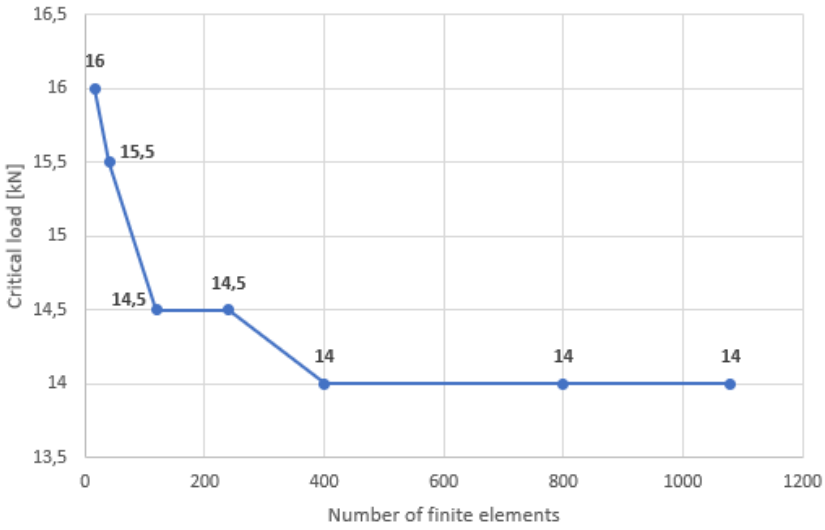

Figure 4.9: Convergence analysis for *Macro_ms* results of the critical load.

4.5 Coupled instability problem – structures built from solids with periodic micro-structure

In this section, some test cases are carried-out for testing the implementation given in chapter 3.1.5.

First, the variation of the critical load with the unit cell's material density (for a given structure and RVE) is studied and compared with the same variation for the macroscopic buckling case. Then, the method is applied to a column with a honeycomb micro-structure.

4.5.1 Critical load factor vs. material density

Here, the variation of the critical load with the unit cell's material density for the coupled instability problem is studied and compared with the same variation for the macroscopic buckling case.

For that purpose, the previous example of a column constrained in both directions on the left side, free on the other side and subjected to a compressing load is considered. This beam has a length $L = 30$m, a height $h = 2$m, a thickness $b = 1$m and it is built from a periodic material characterized by a square RVE of side measuring 0.5m. The unit cell is built from a base material with Young's modulus $E = 2.1$MPa and a Poisson's ratio $\nu = 0.3$. The variation in density for the structure is achieved by varying all RVE's density in the same way: starting from a uniform unit cell (density=1), the density is decreased by introducing a hole in the micro-structure and by progressively increasing the hole's size.

The macroscopic buckling response is obtained by means of the Matlab function *Macro_ms* and the buckling response considering both scales of the problem using the Matlab function *Coupleds*. In both cases, the structure is discretized by the same number of finite elements.

For the macro-scale problem, to obtain the effective material properties, the unit cell is discretized in 10x10 finite elements. Taking this into account, and because the given implementation of the coupled case relies on an equal discretization of both the structures domains, the column is discretized in 24000

finite elements. The density was varied from an initial value of 0.36 up to a final value of 1 and the results of both functions are shown if figure 4.10.

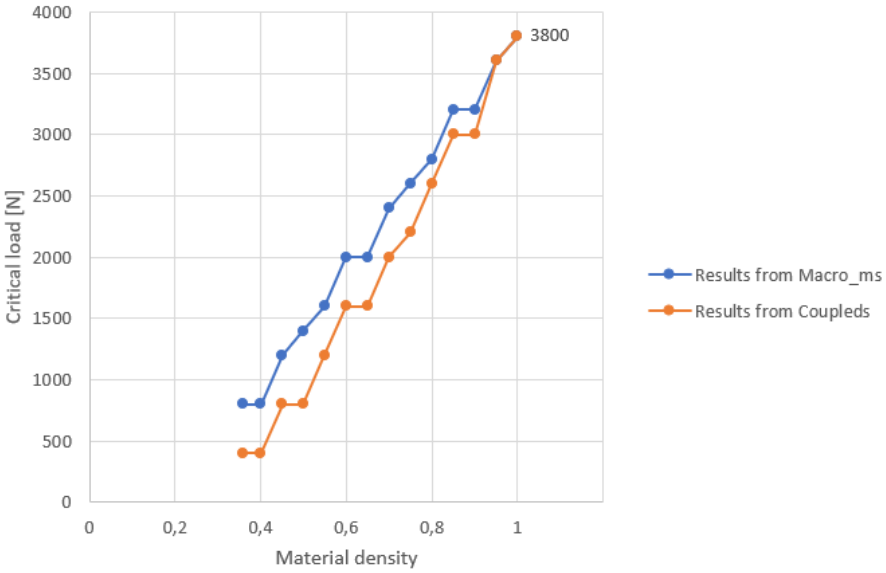

Figure 4.10: Critical load vs. material density – results from *Coupleds* and *Macro_ms*.

For both cases, the decrease of the critical load with decreasing densities is in agreement with the expected decrease in buckling strength as density is reduced.

The case were density is equal to one, corresponds to the case of an homogeneous beam. Therefore, it makes sense that the results from both functions are exactly the same - there is no representative micro-structure to account for. Furthermore, since the used mesh is sufficiently refined, the correspondent buckling load should be, with a small error, the theoretical one given by equation (4.1). This formula gives a theoretical value of 3838.179N, whereas *Coupleds* and *Macro_ms* give 3800N, resulting in an error of less than 1%.

As the density decreases, it is expected, for ”high” values of density, that the buckling response when considering both scales still captures the macro-scale behaviour, since the model still resembles to a homogeneous macro-scale one. In this test, that only happens for density values of 1 and 0.95. For values lower than that, the *Coupleds* function gives a buckling load lower than the one given by *Macro_ms*. This difference in the results from both models is justified, since the elastic properties for elements corresponding to void are null in *Coupleds*, whereas in *Marco_ms* these are homogenized ones.

For all the tested density values, the obtained first and second instability modes are represented in figure 4.11.

As it can be seen, these instability modes are identical to the ones obtained from a macro-scale analysis.

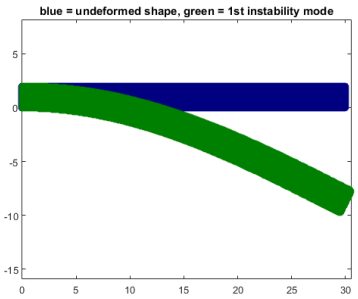

(a) First instability mode

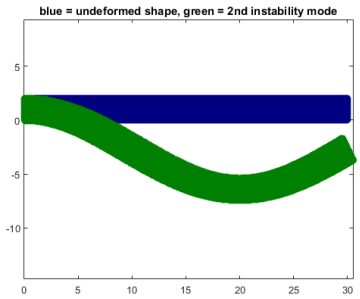

(b) Second instability mode

Figure 4.11: Instability modes' shapes vs. undeformed shape - results from *Coupleds*.

4.5.2 Column with a honeycomb micro-structure

Here, a test case is developed in order to verify if the carried-out implementation of the coupled instability problem can capture micro-scale buckling modes.

Instability phenomena is more likely to happen for cellular materials with lower relative density. Therefore, if the considered implementation can capture instabilities at the micro-scale level, it will do it more easily for materials of this nature, since higher density ones will have a higher buckling strength. As a "low material density" micro-structure, the hexagonal honeycomb is here considered.

To obtain the Y-periodic micro-scale instability behaviour of the honeycomb, the previously mentioned *micro_buckles* function is used. The honeycomb is discretized in 21x12 finite elements and its dimensions are assigned so that the area of the unit cell is one [45]. The base material of this RVE has a Young's molulus $E = 2.1$MPa and a Poisson's ratio ν =0.3 and the void regions are, once again, assigned with null material properties. The unit cell is subjected to a macroscopic strain field of $\varepsilon^0 = C^{te}\{-1\ 0\ 0\}$.

The honeycomb micro-structure and its critical and second buckling modes given by *micro_buckles* can be visualized in figures 4.12 and 4.13, respectively. The results from the *micro_buckles* function showed a critical buckling load factor of 0.0371 (and the corresponding critical load $P_{cr} = 77910$N). This value is much lower than that of any of the feasible micro-structures addressed in section 4.3, meaning that the honeycomb is more suitable than these for the current test case.

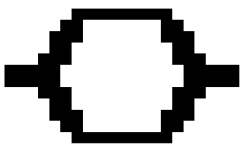

Figure 4.12: Honeycomb micro-structure.

To address the coupled instability problem on a structure with a honeycomb unit cell, a beam constrained in both directions on the left side and subjected to a uniformly distributed loading on the right side, is again considered. The material properties and unit cell's dimensions were kept from the previous

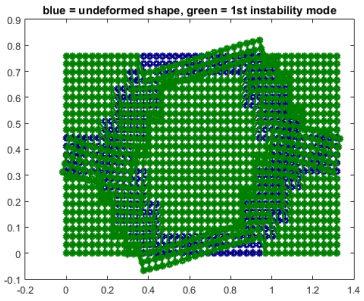

(a) First instability mode for the honeycomb micro-structure

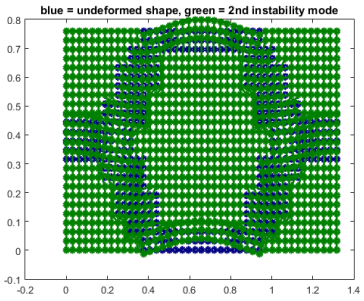

(b) Second instability mode for the honeycomb micro-structure

Figure 4.13: Honeycomb – micro-scale buckling analysis using *micro_buckles*.

micro-scale analysis and the beam's dimensions are L =10.53m, h =3.04m and b =1m.

The structure is discretized in 168x48 finite elements and the analysis is performed by the *Coupleds* function.

As a first analysis, the two first buckling modes/loads are considered. Using *Coupleds*, the obtained values are $P_{cr} = P_1 = 1215.74$N and $P_2 = 3951.15$N, which are much lower than the micro-scale one, indicating that the obtained structure's behaviour at these bifurcation points doesn't exhibit, at least for the entire domain, instabilities on the micro-scale level.

The corresponding mode shapes can be seen in figures 4.14 and 4.15.

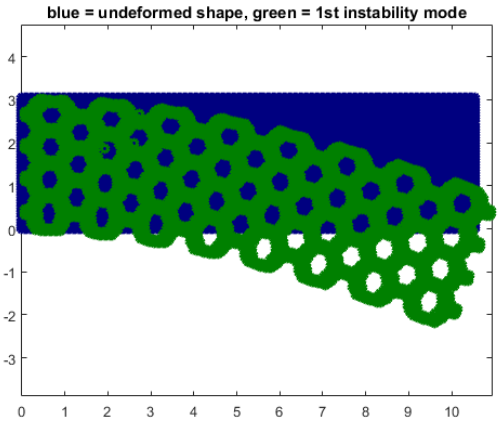

Figure 4.14: Undeformed shape vs. first instability mode shape - beam with honeycomb micro-structure.

The "general" shapes of the two modes are very identical to the ones obtained in the previous analysis concerning the buckling of beams.

In the critical mode shape one cannot identify any buckled unit cell, although it can clearly be seen, specially in the vicinity of the fixed left side, the compressing of the lower cells and the stretching of the upper ones.

For the second instability mode, the previous considerations also apply. However, on the right hand side, where the loading is applied, some unit cells start to buckle (see detail on figure 4.15). While the majority of them resembles the first honeycomb instability mode, the lowest one seems to be on its second one.

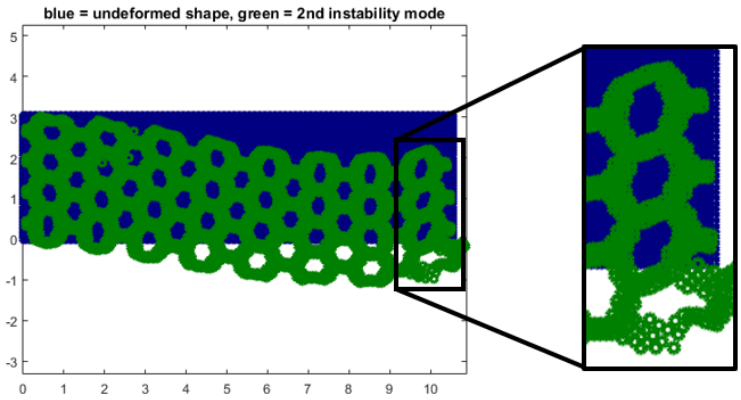

Figure 4.15: Undeformed shape vs. second instability mode shape - beam with honeycomb micro-structure.

Since the so far obtained bifurcation points cause the instability of non or very few unit cells and since the corresponding buckling loads are low when compared to the one obtained from a micro-scale analysis of the honeycomb, it can be expected (or at least worthy of verification), that more cells will become unstable for higher buckling modes.

With that in mind, the calculations from *Coupleds* were extended to obtain the first thirty instability load factors and shapes.

From one bifurcation point to the next, the increase in buckling strength was approximately 300N and the structure exhibited some repeated buckling loads. From this set of buckling loads, none of them exceeded the micro-scale instability load of the honeycomb. However, some of these instability configurations are discussed next, namely $P_{13} = P_{14} = P_{15} = 6382,62$N, $P_{28} = P_{29} = 7902.291$N and $P_{30} = 8206.23$N.

Analyzing the thirteenth instability mode shape (see figure 4.16) , one can see a significant increase in the number of buckled unit cells. These seem to be arranged in columns and subsequent unstable columns seem to be present in the structure in a mirror-like position, resulting in a deformed but not unstable shape for the remaining cells.

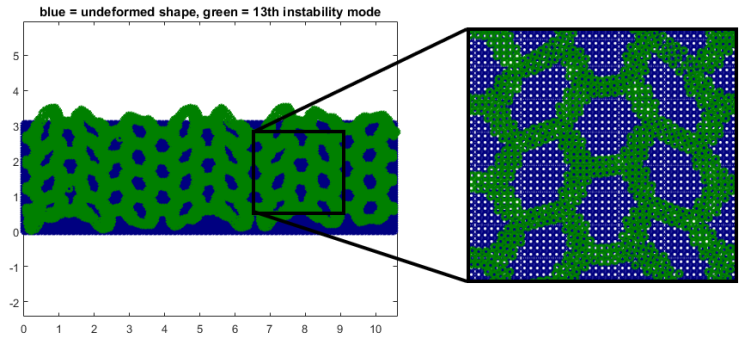

Figure 4.16: Undeformed shape vs. thirteenth instability mode shape - beam with honeycomb micro-structure.

As for the twenty-eightieth buckling configuration in figure 4.17, one can see the appearance of more unit cells exhibiting micro-scale second instability mode shapes, along with some micro-scale first

instability ones as well as with completely stable ones.

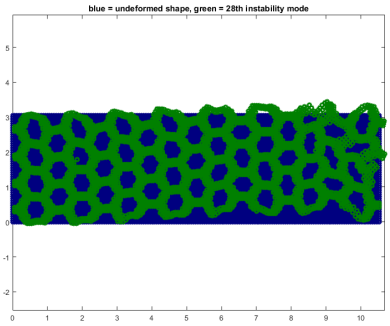

Figure 4.17: Undeformed shape vs. twenty-eightieth instability mode shape - beam with honeycomb micro-structure.

Regarding the thirtieth mode (figure 4.18), it can be observed that no stable cells are present. The majority of them are on their second instability configuration.

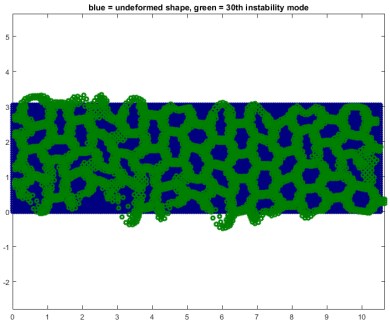

Figure 4.18: Undeformed shape vs. thirtieth instability mode shape - beam with honeycomb micro-structure.

From this test, it can then be concluded that the implementation given by the *Coupleds* function can capture macro-scale as well as micro-scale instabilities. For the analysed structure, the unit cells become unstable, but not in a periodic way and the resultant buckling load never reaches the value of the micro-scale analysis. This last fact is justified, since there is no imposition of periodicity in the boundary conditions.

4.6 Topology optimization for compliance minimization

Here, the default topology optimization for minimum compliance of the MBB beam example presented in [35] is reproduced, using the modified implementation described in section 3.2.1. This is done with the objective of verifying if the insertion of the MMA routines, provided by Prof. Krister Svanberg, into the implementation from [35] was, in this work, done correctly and examining the convergence of the solution.

In [35], using boundary conditions to account for the symmetry of the structure, only half of the MBB beam is optimized. Furthermore, the load, pointing downwards and vertically, is applied to the upper left

corner and the beam is horizontally supported in the lower right corner.

The used inputs correspond to the ones of the first presented mesh in [35]: 60 elements in the $x-$ direction, 20 elements in the $y-$ direction, a volume fraction of 0.50, a filter radius of 2.4, a penalization factor of 3 and the density filter was chosen as the filtering technique (ft=2).

The results for the topology of the optimized MBB beam as well as the compliance history during the optimization process are shown in figures 4.19 and 4.20, respectively.

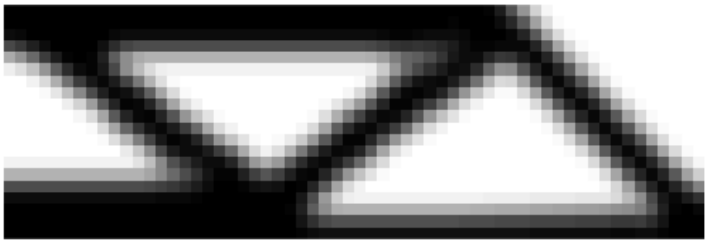

Figure 4.19: Obtained optimal solution for minimum compliance of the MBB beam.

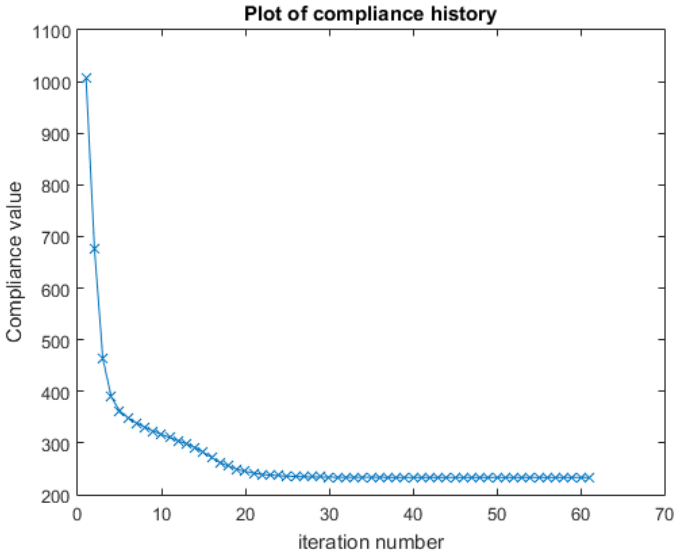

Figure 4.20: Compliance history for the optimization of the MBB beam.

The obtained topology agrees very well with the corresponding one presented in [35], from a direct comparison between the two. Furthermore, the value of the compliance converges to a minimum value throughout the optimization process. As it can be seen in figure 4.20, the solution was obtained after approximately 60 iterations, although it converges to its final value sooner than that (around 40 iterations). The criterion to end the optimization process, which is based on the maximum difference in consecutive design variables and assigned a value of 0.01, could then be assigned a higher value in order to stop the process at a lower iteration number with a still converged result.

This simple test indicates, then, that the MMA method was successfully included as the updating scheme for the design variables.

4.7 Topology optimization for buckling strength maximization

In this section, a simple example of beam, fixed in left hand side and subjected to a horizontally distributed compressing load on the right hand side, is optimized for maximum buckling strength using the developed Matlab function *TopOptBuckling*. The beam's dimensions are L=20m, h=5m and b=1m and the applied load has a value of 1Pa. The structure is discretized into 30x8 finite elements and the material parameters, following the notation in chapter 2.3.2, are E_1=1Pa, $E_0 = 10^{-6}$Pa and the Poisson's ratio is ν=0.3.

The structure is optimized for a maximum allowed total volume fraction of 0.6. The penalization factor used in the SIMP curves is p=3 and filter radius has a value of 0.2m. The tolerance parameter regarding the convergence criterion (which is based on consecutive changes of the design variables) was assigned to be 0.01.

The results for the optimized topology of the beam as well as the objective function's history during the optimization iterations are shown in figures 4.21 and 4.22, respectively,

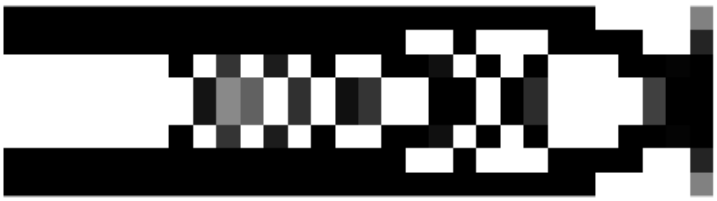

Figure 4.21: Obtained optimal solution for maximum buckling strength of the column after 49 iterations.

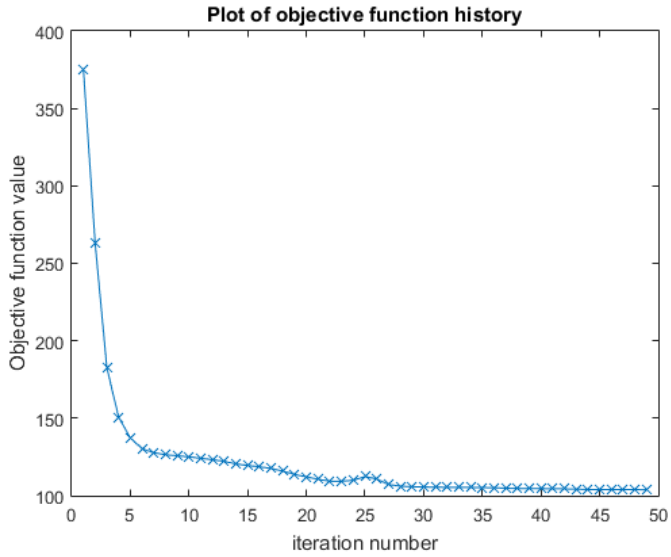

Figure 4.22: Objective function history for the optimization of the column.

From figure 4.22, it can be seen that the objective function converges to a solution throughout the optimization process with only one oscillation. Furthermore, the critical buckling load is raised from 2.66×10^{-3}N up to a final value of 9.63×10^{-3}N, which represents a raise of 266% from the uniform

material distribution case.

The final topology (see figure 4.21) presents some areas that can be identified as the so called (and to be avoided) checker-board patterns. However, the solid areas of these regions seem to be aligned with each other, suggesting that these patterns are present due to the poor refinement of the mesh.

Chapter 5

Conclusions

Structural topology optimization has been a hot topic over the last decades in the research community. In recent years a renewed interest on topology optimization addressing buckling behavior has been observed, due to the inherent difficulties of the problem. These problems have, although not very extensively, already been studied at separated macro- and micro- scales. However, as this dissertation shows, structures can, in some cases, exhibit simultaneous-scale buckling modes, which has not been addressed in topology optimization of structures.

This work provides, then, some investigations in numerical implementations to be used in topology optimization of structures (macro-scale) and micro-structures (micro-scale) for linearized buckling performance maximization as well as the first implementation steps to be carried-out when performing this type of optimization procedure.

5.1 Achievements

The finite element approximations to treat the linearized stability problem at macro-scale, micro-scale as well as mixed-scale are here reviewed.

For the case of structures built from cellular periodic materials, the implementations of the stability problems at separated macro- and micro-scales were verified with simple yet illustrative examples from the literature, including the necessary implementation of the homogenization method.

Furthermore, it is proposed, in this work, a model for the coupled-scale stability problem, which seems to be able to capture macro-scale as well as micro-scale behaviours, at least for the presented examples. This is the first attempt to implement and analyze this coupled scale model, as far as the author knows.

Moreover, the developed implementation for the maximization of the buckling strength of structures converges to an optimal solution.

5.2 Future Work

The implementations to solve the stability problem at separated macro-scale and micro-scale are suitable and can be extended to perform homogenization based topology optimization of structures (macro-scale) and micro-structures (micro-scale) for maximum buckling strength.

For the case of the micro-scale buckling response, the implementation here given is limited to the assumption of Y-periodicity of the buckling modes, which can be further generalized for modes with other wave-lengths using the Bloch-wave theory.

Furthermore, in resultant applications of the methods (3D prints, infill structures,...), investigations on scale and boundary effects due to the presence of a finite repetition of a periodic unit cell could be made.

The given implementation of the coupled-scale instability problem can be further reviewed, namely regarding the validity of using the same discretization for the macro- and micro- domains and the computational efficiency. Furthermore, if this implementation is proven to be valid, since it relies on an equal discretization of the micro- and macro-domains, it could, perhaps, be used in a topology optimization problem to maximize the critical coupled-buckling load of structures. However, since it is developed for structures built from periodic cellular materials, this would possibly require the addition of further constraints on the design variables to ensure the periodicity of the unit cell's topology.

Moreover, the simplified implementation given for the density based topology optimization for maximized buckling strength yields a basis for including the problem of non-differentiability of the objective function for repeated buckling loads.

References

[1] C. R. Thomsen, F. Wang, and O. Sigmund. Buckling strength topology optimization of 2d periodic materials based on linearized bifurcation analysis. *Comput. Methods Appl. Mech. Engrg.*, May 2018. https://doi.org/10.1016/j.cma.2018.04.031.

[2] T. W. Chin and G. J. Kennedy. Large-scale compliance minimization and buckling topology optimization of the undeformed common research model wing. In *AIAA SciTechForum*, 2016.

[3] V. O. Balabanov and R. T. Hafka. Topology optimization of transport wing internal structure. In *AIAA-94-4414-CP*, 1994.

[4] D. Liu, C. Zhang, Z. Wan, and Z. Du. Topology optimization of a novel fuselage structure in the conceptual design phase. *Aircraft Engineering and Aerospace Technology*, 2018. https://doi.org/10.1108/AEAT-04-2017-0100.

[5] M. Raheel and V. Toropov. Topology optimization of an aircraft wing with an outboard x-stabilizer. In *AIAA AVIATION Forum*, 2018.

[6] G. Singh and V. Toropov. Topology optimization of a blended-wing-body aircraft structure. In *AIAA AVIATION Forum*, 2016.

[7] E. Oktay, H. Akay, and O. Merttopcuoglu. Parallelized structural topology optimization and cfd coupling for design of aircraft wing structures. *Computers Fluids*, 49:141–145, 2011.

[8] K. A. James, G. J. Kennedy, and J. R. R. A. Martins. Concurrent aerostructural topology optimization of a wing box. *Computers and Structures*, 134:1–17, 2014.

[9] D. J. Munk, D. J. Auld, G. P. Steven, and G. A. Vio. On the benefits of applying topology optimization to structural design of aircraft components. *Structural and Multidisciplinary Optimization*, 2019.

[10] L. Krog, A. Tucker, M. Kemp, and R. Boyd. Topology optimization of aircraft wing box ribs. In *10th AIAA/ISSMO Multidisciplinary Analysis and Optimization Conference*, 2004.

[11] F. Ferrari and O. Sigmund. Revisiting topology optimization with buckling constraints. *Structural and Multidisciplinary Optimization*, 59:1401–1415, 2019. https://doi.org/10.1007/s00158-019-02253-3.

[12] M. M. Neves, O. Sigmund, and M. P. Bendsøe. Topology optimization of periodic microstructures with a penalization of highly localized buckling modes. *International Journal for Numerical Methods in Engineering*, 54:809–834, 2002. DOI: 10.1002/nme.449.

[13] M. M. Neves, O. Sigmund, and M. Bendsøe. Topology optimization of periodic microstructures with a buckling criteria. In *Fifth World Congress on Computational Mechanics*, Vienna University of Technology, Austria, 2002.

[14] H. C. Rodrigues, J. M. Guedes, and M. P. Bendsøe. Necessary conditions for optimal design of structures with a nonsmooth eigenvalue based criterion. *Structural Optimization*, 9:52–56, 1995.

[15] M. M. Neves, H. Rodrigues, and J. M. Guedes. Generalized topology design of structures with a buckling load criterion. *Structural Optimization*, 10:71–78, 1995.

[16] M. M. Neves. Symbolic computation to derive a linear-elastic buckling theory for solids with periodic microstructure. *International Journal for Computational Methods in Engineering Science and Mechanics*, March 2019. DOI: 10.1080/15502287.2019.1566286.

[17] S. Hollister and N. Kikuchi. A comparison of homogenization and standard mechanics analyses for periodic porous composites. In *Computational Mechanics*, volume 10, pages 73–95. Springer-Verlag, 1992.

[18] A. Mota, I. Tezaur, and C. Alleman. The schwarz alternating method in solid mechanics. *Comput. Methods Appl. Mech. Engrg.*, 319:19–51, 2017.

[19] K. Liu and A. Tovar. An efficient 3d topology optimization code written in matlab. In *Structural and Multidisciplinary Optimization*, volume 50, pages 1175–1196. Springer-Verlag, 2014. DOI:10.1007/s00158-014-1107-x.

[20] B. Hassani and E. Hinton. A review of homogenization and topology optimization i - homogenization theory for media with periodic structure. *Computers and Structures*, 69:707–717, 1998.

[21] B. Hassani and E. Hinton. A review of homogenization and topology optimization ii - analytical and numerical solution of homogenization equations. *Computers and Structures*, 69:719–738, 1998.

[22] B. Hassani and E. Hinton. A review of homogenization and topology optimization iii - topology optimization using optimality criteria. *Computers and Structures*, 69:739–756, 1998.

[23] P. W. Christensen and A. Klarbring. *An Introduction to Structural Optimization*. Springer, 2008.

[24] M. P. Bendsøe and O. Sigmund. *Topology optimization: theory, methods and applications*. Springer, 2nd edition, 2003.

[25] F. Ferrari and O. Sigmund. Towards solving large-scale topology optimization problems with buckling constraints at the cost of linear analysis. *Comput. Methods Appl. Mech. Engrg.*, 363, 2020.

[26] M. M. Neves. Otimização da topologia de estruturas com constrangimentos de estabilidade. Master's thesis, Instituto Superior Técnico, April 1994.

[27] Y. Fung. *A First Course in Continuum Mechanics for Physical and Biological Engineers and Scientists*. Simon Schuster Company, 3rd edition, 1994.

[28] S. Timoshenko and J. N. Goodier. *Theory of Elasticity*. 2nd edition, 1951.

[29] J. Reddy. *An Introduction to the Finite Element Method*. 3rd edition, 2006.

[30] J. Fish and T. Belytschko. *A First Course in Finite Elements*. John Wiley Sons, 2007.

[31] A. Bensoussan, J. L. Lions, and G. Papanicolaou. *Asymptotic analysis for periodic structures*, volume 5. North-Holand Publishing Company, 1978.

[32] J. M. Guedes and N. Kikuchi. Preprocessing and postprocessing for materials based on the homogenization method with adaptive finite element methods. *Computer Methods in Applied Mechanics and Engineering*, 83:143–198, 1990.

[33] O. Sigmund. A 99 topology optimization code written in matlab. In *Structural and Multidisciplinary Optimization*, volume 21, pages 120–127. Springer-Verlag, 2001.

[34] O. Sigmund. Morphology-based black and white filters for topology optimization. *Struct. Multidisc. Optim.*, 33:401–424, 2007.

[35] E. Andreassen, A. Clausen, M. Schevenels, B. Lazarov, and O. Sigmund. Efficient topology optimization in matlab using 88 lines of code. In *Structural and Multidisciplinary Optimization*, volume 43, pages 1–16. Springer-Verlag, 2011.

[36] K. Svanberg. The Method of Moving Asymptotes - a new method for structural optimization. *International Journal for Numerical Methods in Engineering*, 24:359–373, 1987.

[37] F. Ferrari and O. Sigmund. A new generation 99 line matlab code for compliance topology optimization and its extension to 3d. *Structural and Multidisciplinary Optimization*, 62:2211–2228, 2022.

[38] T. E. Bruns and D. A. Tortorelli. Topology optimization of non-linear elastic structures and compliant mechanisms. *Comput. Methods Appl. Mech. Engrg.*, 190:3443–3459, 2001.

[39] B. Bourdin. Filters in topology optimization. *Int. J. Numer. Meth. Engrg*, 50:2143–2158, 2001.

[40] X. Gao and H. Ma. Topology optimization of continuum structures under buckling constraints. *Comput. Struct.*, 157:142–152, 2015.

[41] E. Andreassen and C. S. Andreasen. How to determine composite material properties using numerical homogenization. *Computational Materials Science*, 83:488–495, 2014. https://doi.org/10.1016/j.commatsci.2013.09.006.

[42] K. Svanberg. MMA and GCMMA - two methods for nonlinear optimization.

[43] M. P. Bendsøe and N. Kikuchi. Generating optimal topologies in structural design using a homogenization method. *Computer Methods in Applied Mechanics and Engineering*, 71:197–224, 1988.

[44] S. Timoshenko and J. Gere. *Theory of Elastic Stability*. 2nd edition, 1985.

[45] O. Sigmund. *Design of material structures using topology optimization*. PhD thesis, Technical University of Denmark, 1994.

Appendix A

Geometric stiffness matrices for plane elasticity problems

A.1 Micro-scale geometric stiffness matrix

In matrix form, given the approximation of the instability modes by means their nodal values and the nodal shape functions, the second integral in equation 2.67

$$\int_{\#Y} \sigma^0_{km} \frac{\partial \phi_c}{\partial y_k} \frac{\partial \psi_c}{\partial y_m} dY \text{ becomes } \boldsymbol{\phi}^T \boldsymbol{G_y} \boldsymbol{\phi}, \tag{A.1}$$

where the geometric stiffness matrix $\boldsymbol{G_y}$ results from the assembly of the elemental ones given by

$$\boldsymbol{G_y}^e = \int_{\Omega_e} \boldsymbol{g}_e^T \boldsymbol{\sigma}^0_e \boldsymbol{g}_e d\Omega. \tag{A.2}$$

The matrix $\boldsymbol{g}_e$ is defined by [40]

$$\boldsymbol{g}_e = \begin{bmatrix} \frac{\partial N_1}{\partial y_1} & 0 & ... & \frac{\partial N_n}{\partial y_1} & 0 \\ \frac{\partial N_1}{\partial y_2} & 0 & ... & \frac{\partial N_n}{\partial y_2} & 0 \\ 0 & \frac{\partial N_1}{\partial y_1} & ... & 0 & \frac{\partial N_n}{\partial y_1} \\ 0 & \frac{\partial N_1}{\partial y_2} & ... & 0 & \frac{\partial N_n}{\partial y_2} \end{bmatrix}, \tag{A.3}$$

with n denoting the number of nodes per element.

The initial stress matrix is

$$\boldsymbol{\sigma}^0_e = \begin{bmatrix} \sigma_{11} & \sigma_{12} & 0 & 0 \\ \sigma_{12} & \sigma_{22} & 0 & 0 \\ 0 & 0 & \sigma_{11} & \sigma_{12} \\ 0 & 0 & \sigma_{12} & \sigma_{22} \end{bmatrix}, \tag{A.4}$$

where the initial stress components, from equation 2.68 are given by [1]

$$\begin{Bmatrix} \sigma_{11} \\ \sigma_{22} \\ \sigma_{12} \end{Bmatrix}_e = \boldsymbol{E}_e(\boldsymbol{I} - \boldsymbol{B}_e\boldsymbol{\chi}_e)\boldsymbol{e}_e \tag{A.5}$$

In the previous equation $\boldsymbol{I}$ is the identity matrix, $\boldsymbol{\chi}_e = [\chi_e^1\ \chi_e^2\ \chi_e^3]$ is a $3 \times n$ matrix containing the characteristic displacement fields and $\boldsymbol{e}_e$ is the macroscopic strain field.

A.2 Macro-scale geometric stiffness matrix

The macro-scale geometric stiffness matrix is obtained in the same fashion as the previous case, taking only into considerations that the initial stress components, from equation 2.70, are now given by

$$\begin{Bmatrix} \sigma_{11} \\ \sigma_{22} \\ \sigma_{12} \end{Bmatrix}_e = \boldsymbol{E}_e^H\boldsymbol{e}_e. \tag{A.6}$$

Appendix B

Calculation of the adjoint force

The component i of the adjoint force

$$\begin{Bmatrix} \boldsymbol{\phi}_{cr}^T \frac{\partial \boldsymbol{G}}{\partial u_1} \boldsymbol{\phi}_{cr} \\ \dots \\ \boldsymbol{\phi}_{cr}^T \frac{\partial \boldsymbol{G}}{\partial u_d} \boldsymbol{\phi}_{cr} \end{Bmatrix} \tag{B.1}$$

is obtained from the global nodal instability vector $\boldsymbol{\phi}_{cr}$ the assemblage of $\frac{\partial \boldsymbol{G}_e}{\partial u_i}$.

From the equations for the calculation of the stiffness matrices in Appendix A,

$$\boldsymbol{G}^e = \int_{\Omega_e} \boldsymbol{g}_e^T \boldsymbol{\sigma}_e^0 \boldsymbol{g}_e d\Omega, \tag{B.2}$$

where $\boldsymbol{\sigma}_e^0$ is obtained by a rearrangement of the components of the stress tensor $\boldsymbol{\sigma}_e = \boldsymbol{E}_e \boldsymbol{B}_e \boldsymbol{u}_e$.

Therefore, for the i-th global degree of freedom, $\frac{\partial \boldsymbol{G}_e}{\partial u_i}$ is

$$\frac{\partial \boldsymbol{G}_e}{\partial u_i} = \int_{\Omega_e} \boldsymbol{g}_e^T \frac{\partial \boldsymbol{\sigma}_e^0}{\partial u_i} \boldsymbol{g}_e d\Omega, \tag{B.3}$$

where $\frac{\partial \boldsymbol{\sigma}_e^0}{\partial u_i}$ is obtained by the rearrangement of

$$\frac{\partial \boldsymbol{\sigma}_e^0}{\partial u_i} = \boldsymbol{E}_e \boldsymbol{B}_e \frac{\partial \boldsymbol{u}_e}{\partial u_i}. \tag{B.4}$$

Thus, when i is a degree of freedom of element e, then the corresponding entry of $\frac{\partial \boldsymbol{u}_e}{\partial u_i}$, given by the correspondent node number of the master element, is 1 and the remaining ones are zero.

Appendix C

Scripts: equations for elastic buckling

The following symbolic computation scripts were used to review the equations obtained in [16] for the static elastic buckling model for structures with periodic micro-structure.

```
%%%%%%%%%%%%%%%%%%%%%%%%%%%%%%%%%%%%%%%%%%%%%%%%%%
%Script 01: input is (1) and (7) and output is (8)
%%%%%%%%%%%%%%%%%%%%%%%%%%%%%%%%%%%%%%%%%%%%%%%%%%
syms duxyij duxyji duxyki duxykj
syms alpha du0xyij du1xyij du0xyji du1xyji du0xyki du1xyki du0xykj du1xykj
syms epson
syms du00xyij du00xyiJ du10xyij du10xyiJ du00xyji du00xyjI du10xyji du10xyjI
syms du00xyki du00xykI du10xyki du10xykI du00xykj du00xykJ du10xykj du10xykJ
syms du01xyij du01xyiJ du11xyij du11xyiJ du01xyji du01xyjI du11xyji du11xyjI
syms du01xyki du01xykI du11xyki du11xykI du01xykj du01xykJ du11xykj du11xykJ
%Note: when indices are represented with capital letters, the derivative is
%with respect to y; when they are not, they are with respect to x
%%%%%%%%%%%%%%%%%%%%%%%%%%%%%%%%%%%%%%%%%%%%%%%%%%%%%%%%%%%%%%%%%%%%%%%%%%%
%Buckling requires 2nd order term of strain
eij=1/2*(duxyij+duxyji)+1/2*(duxyki*duxykj);
%The bifurcation is characterized by u=u0+alfa*u1
eij2=subs(eij, {duxyij,duxyji,duxyki,duxykj},...
               {du0xyij+alpha*du1xyij, du0xyji+alpha*du1xyji,...
                du0xyki+alpha*du1xyki,du0xykj+alpha*du1xykj});
eij3=expand(eij2);
eij4=collect(eij3,alpha);
eija=sort(eij4);
%%%%%%%%%%%%%%%%%%%%%%%%%%%%%%%%%%%%%%%%%%%%%%%%%%
%Script 02: input is (9-12) and output is (13-14)
%%%%%%%%%%%%%%%%%%%%%%%%%%%%%%%%%%%%%%%%%%%%%%%%%%
eijs=simplify(eij3-1/2*du0xyki*du0xykj-alpha/2*(du0xykj*du1xyki+du1xykj*du0xyki)); %(9)
%Introducing (10), (11) and (12)
eijsB=expand(subs(eijs, {du0xyij, ...
                   du1xyij, ...
                   du0xyji, ...
                   du1xyji, ...
                   du1xyki, ...
                   du1xykj},...
                  {du00xyij+1/epson*du00xyiJ+epson*(du01xyij+1/epson*du01xyiJ),...
                   du10xyij+1/epson*du10xyiJ+epson*(du11xyij+1/epson*du11xyiJ),...
                   du00xyji+1/epson*du00xyjI+epson*(du01xyji+1/epson*du01xyjI),...
                   du10xyji+1/epson*du10xyjI+epson*(du11xyji+1/epson*du11xyjI),...
                   du10xyki+1/epson*du10xykI+epson*(du11xyki+1/epson*du11xykI),...
                   du10xykj+1/epson*du10xykJ+epson*(du11xykj+1/epson*du11xykJ)}));
[eijsBB,terms]=coeffs(eijsB, alpha);
%Obtaining equations (14)
eijsB0=sort(collect(expand(eijsBB(terms == 1)),epson));
eijsB1=sort(collect(expand(eijsBB(terms == alpha)),epson));
```

```
eijsB2=sort(collect(expand(eijsBB(terms == alpha^2)),epson));

%%%%%%%%%%%%%%%%%%%%%%%%%%%%%%%%%%%%%%%%%%%%%%%%%%%%%%%%%%%%%%%%%%%%%%%%%%%%%%%
%Script 03: input is (14.1), (14.2) and (16) and output is integrFxy1
%%%%%%%%%%%%%%%%%%%%%%%%%%%%%%%%%%%%%%%%%%%%%%%%%%%%%%%%%%%%%%%%%%%%%%%%%%%%%%%
syms epson Eijkm
syms du00xyiJ du00xyjI du00xyij du00xyji du01xyiJ du01xyjI du01xyij du01xyji
syms du10xyiJ du10xyjI du10xyij du10xyji du11xyiJ du11xyjI du11xyij du11xyji
syms dv00xyiJ dv00xyjI dv00xyij dv00xyji dv01xyiJ dv01xyjI dv01xyij dv01xyji
syms dv10xyiJ dv10xyjI dv10xyij dv10xyji dv11xyiJ dv11xyjI dv11xyij dv11xyji
syms du00xykM du00xymK du00xykm du00xymk du01xykM du01xymK du01xykm du01xymk
syms du10xykM du10xymK du10xykm du10xymk du11xykM du11xymK du11xykm du11xymk
syms dv00xykM dv00xymK dv00xykm dv00xymk dv01xykM dv01xymK dv01xykm dv01xymk
syms dv10xykM dv10xymK dv10xykm dv10xymk dv11xykM dv11xymK dv11xykm dv11xymk
%Note: when indices are represented with capital letters, the derivative is
%with respect to y; when they are not, they are with respect to x
%%%%%%%%%%%%%%%%%%%%%%%%%%%%%%%%%%%%%%%%%%%%%%%%%%%%%%%%%%%%%%%%%%%%%%%%%%%%%%%
%Calculation of the integrand of the first integral of eq. (16): integrFxy1
eijsB0_sum=2*((du01xyij)*epson+(du01xyiJ+du00xyij)+(du00xyiJ)/epson)/(2);
eijsB0_sumV=0;
ekmsB0_sum=2*((du01xykm)*epson+(du01xykM+du00xykm)+(du00xykM)/epson)/(2);
ekmsB0_sumV=0;
eijsB1_sum=2*((du11xyij)*epson+(du11xyiJ+du10xyij)+(du10xyiJ)/epson)/(2);
eijsB1_sumV=2*((dv11xyij)*epson+(dv11xyiJ+dv10xyij)+(dv10xyiJ)/epson)/(2);
ekmsB1_sum=2*((du11xykm)*epson+(du11xykM+du10xykm)+(du10xykM)/epson)/(2);
ekmsB1_sumV=2*((dv11xykm)*epson+(dv11xykM+dv10xykm)+(dv10xykM)/epson)/(2);

integrFxy1=collect(expand(Eijkm*(eijsB0_sum*ekmsB1_sumV+eijsB0_sumV*ekmsB1_sum))
    ,epson);
%
    %%%%%%%%%%%%%%%%%%%%%%%%%%%%%%%%%%%%%%%%%%%%%%%%%%%%%%%%%%%%%%%%%%%%%%%%%%%%%%%

%Script 3a: input is (16)and integrFxy1 and output is the integrand of (18) and
    (19)
%
    %%%%%%%%%%%%%%%%%%%%%%%%%%%%%%%%%%%%%%%%%%%%%%%%%%%%%%%%%%%%%%%%%%%%%%%%%%%%%%%

integrFxy1a=collect(integrFxy1*(epson^2),epson); %Needed because integrFxy1
    appears devided by epson^2, which
[IntFxy1b,terms]=coeffs(integrFxy1a, epson);     %prevents a proper collection
    of the coefficients
EM2=IntFxy1b(terms == 1); %integrand of (18)
%%%%%%%%%%%%%%%%%%%%%%%%%%%%%%%%%%%%%%%%%%%%%%%%%%%%%%%%%%%%%%%%%%%%%%%%%%%%%%%
%Script 3b: input is (16) and integrFxy1 and output is (20-22)
%%%%%%%%%%%%%%%%%%%%%%%%%%%%%%%%%%%%%%%%%%%%%%%%%%%%%%%%%%%%%%%%%%%%%%%%%%%%%%%
EM1=IntFxy1b(terms == epson); %integrand of (20)
EM1v11=expand(subs(EM1,{dv10xykM,dv10xykm},{0,0})); %v10=0 => eq.(19)
EM1v10=expand(subs(EM1,{dv11xykM,du00xyiJ},{0,0})); %v11=0 + eq.(19) =>
    integrand of eq.(21)
%%%%%%%%%%%%%%%%%%%%%%%%%%%%%%%%%%%%%%%%%%%%%%%%%%%%%%%%%%%%%%%%%%%%%%%%%%%%%%%
%Script 3c: input is (16) and integrFxy1 and output is (25-29)
%%%%%%%%%%%%%%%%%%%%%%%%%%%%%%%%%%%%%%%%%%%%%%%%%%%%%%%%%%%%%%%%%%%%%%%%%%%%%%%
EM0=IntFxy1b(terms == epson^2); %before using eq.(19) and (32)
EM0_25=EM0-Eijkm*du00xyiJ*dv11xykm-Eijkm*du01xyij*dv10xykM; %integrand of eq
    .(25)
EM0v10=expand(subs(EM0_25,{dv11xykM},{0})); %eq.26
%%%%%%%%%%%%%%%%%%%%%%%%%%%%%%%%%%%%%%%%%%%%%%%%%%%%%%%%%%%%%%%%%%%%%%%%%%%%%%%
%Script 3d: input is (16) and integrFxy1 and output is (30-32)
%%%%%%%%%%%%%%%%%%%%%%%%%%%%%%%%%%%%%%%%%%%%%%%%%%%%%%%%%%%%%%%%%%%%%%%%%%%%%%%
Ep1=IntFxy1b(terms == epson^3);
Ep1v10=expand(subs(Ep1,{dv11xykm,dv11xykM},{0,0})); %integrand of eq.(31)
Ep1v11=expand(subs(Ep1,{dv10xykm},{0})); %returns ~ eq. (26), leading again to
    eq.(29)
%%%%%%%%%%%%%%%%%%%%%%%%%%%%%%%%%%%%%%%%%%%%%%%%%%%%%%%%%%%%%%%%%%%%%%%%%%%%%%%
%Script 04: input is script 03, (14.3) and (17) and output is integrFxy2
%%%%%%%%%%%%%%%%%%%%%%%%%%%%%%%%%%%%%%%%%%%%%%%%%%%%%%%%%%%%%%%%%%%%%%%%%%%%%%%
syms du11xyci du11xycj du11xycI du11xycJ du10xycj du10xyci du10xycJ du10xycI
syms du11xyck du11xycm du11xycK du11xycM du10xycm du10xyck du10xycM du10xycK
syms dv11xyck dv11xycm dv11xycK dv11xycM dv10xycm dv10xyck dv10xycM dv10xycK
%Note: when indices are represented with capital letters, the derivative is
%with respect to y; when they are not, they are with respect to x
%%%%%%%%%%%%%%%%%%%%%%%%%%%%%%%%%%%%%%%%%%%%%%%%%%%%%%%%%%%%%%%%%%%%%%%%%%%%%%%
%Calculation of the integrand of the integral of eq. (17): integrFxy2
```

```
eijsB2=(1/2)*du11xyci*du11xycj*epson^2+...
       (1/2)*du11xycI*du11xycj*epson+...
       (1/2)*du11xyci*du11xycJ*epson+...
       (1/2)*du11xyci*du10xycj*epson+...
       (1/2)*du10xyci*du11xycj*epson+...
       (1/2)*du10xyci*du10xycJ/epson+...
       (1/2)*du11xycI*du10xycJ/epson+...
       (1/2)*du10xycI*du11xycJ/epson+...
       (1/2)*du10xycI*du10xycj/epson+...
       (1/2)*du10xycI*du10xycJ/epson^2+...
       (1/2)*du10xycI*du11xycj+...
       (1/2)*du10xyci*du11xycJ+...
       (1/2)*du11xycI*du10xycj+...
       (1/2)*du10xyci*du10xycj+...
       (1/2)*du11xyci*du10xycJ+...
       (1/2)*du11xycI*du11xycJ;

ekmsB2_V=(1/2)*du11xyck*du11xycj*epson^2+(1/2)*dv11xyck*dv11xycm*epson^2+...
         (1/2)*du11xycK*dv11xycm*epson+(1/2)*dv11xycK*du11xycm*epson+...
         (1/2)*du11xyck*dv11xycM*epson+(1/2)*dv11xyck*du11xycM*epson+...
         (1/2)*du11xyck*dv10xycm*epson+(1/2)*dv11xyck*du10xycm*epson+...
         (1/2)*du10xyck*dv11xycm*epson+(1/2)*dv10xyck*du11xycm*epson+...
         (1/2)*du10xyck*dv10xycM/epson+(1/2)*dv10xyck*du10xycM/epson+...
         (1/2)*du11xycK*dv10xycM/epson+(1/2)*dv11xycK*du10xycM/epson+...
         (1/2)*du10xycK*dv11xycM/epson+(1/2)*dv10xycK*du11xycM/epson+...
         (1/2)*du10xycK*dv10xycm/epson+(1/2)*dv10xycK*du10xycm/epson+...
         (1/2)*du10xycK*dv10xycM/epson^2+(1/2)*dv10xycK*du10xycM/epson^2+...
         (1/2)*du10xycK*dv11xycm+(1/2)*dv10xycK*du11xycm+...
         (1/2)*du10xyck*dv11xycM+(1/2)*dv10xyck*du11xycM+...
         (1/2)*du11xycK*dv10xycm+(1/2)*dv11xycK*du10xycm+...
         (1/2)*du10xyck*dv10xycm+(1/2)*dv10xyck*du10xycm+...
         (1/2)*du11xyck*dv10xycM+(1/2)*dv11xyck*du10xycM+...
         (1/2)*du11xycK*dv11xycM+(1/2)*dv11xycK*du11xycM;

integrFxy2=collect(expand(Eijkm*(eijsB0_sum*ekmsB2_V+eijsB0_sumV*eijsB2+
    eijsB1_sumV*ekmsB1_sum+eijsB1_sum*ekmsB1_sumV)),epson);
%%%%%%%%%%%%%%%%%%%%%%%%%%%%%%%%%%%%%%%%%%%%%%%%%%%%%%%%
%Script 4a: input is integrFxy2 and output is (33)
%%%%%%%%%%%%%%%%%%%%%%%%%%%%%%%%%%%%%%%%%%%%%%%%%%%%%%%%
integrFxy2a=collect(integrFxy2*(epson^3),epson); %Needed because integrFxy2
    appears devided by epson^3, which
[IntFxy2b,trms]=coeffs(integrFxy2a, epson);      %prevents a proper collection
    of the coefficients
Em3=IntFxy2b(trms == 1); %integrand of (33)
%%%%%%%%%%%%%%%%%%%%%%%%%%%%%%%%%%%%%%%%%%%%%%%%%%%%%%%%%%%%%%%%%%%%%%%%
%Script 4b: input is integrFxy2 and output is (34-37)
%%%%%%%%%%%%%%%%%%%%%%%%%%%%%%%%%%%%%%%%%%%%%%%%%%%%%%%%%%%%%%%%%%%%%%%%
Em2=IntFxy2b(trms == epson);
Em2v10=expand(subs(Em2,{dv11xycM,dv11xycK,du00xyiJ},{0,0,0})); %v11=0 + eq.(19)
    => integrand of eq. (34)
%%%%%%%%%%%%%%%%%%%%%%%%%%%%%%%%%%%%%%%%%%%%%%%%%%%%%%%%%%%%%%%%%%%%%%%%
%Script 4c: input is integrFxy2 and output is (38-40)
%%%%%%%%%%%%%%%%%%%%%%%%%%%%%%%%%%%%%%%%%%%%%%%%%%%%%%%%%%%%%%%%%%%%%%%%
Em1=IntFxy2b(trms == epson^2);
Em1a=expand(subs(Em1,{du00xyiJ},{0})); % Aplication of eq. (19) to Em1
Em1v11=expand(subs(Em1a,{dv10xykM,dv10xyiJ,dv10xykm,dv10xyij,dv10xycM,dv10xycK,
    dv10xycm,dv10xyck},...
        {0,0,0,0,0,0,0,0})); %v10=0 => eq. (38)
Em1v10=expand(subs(Em1a,{dv11xykM,dv11xyiJ,dv11xycM,dv11xycK},{0,0,0,0})); %v11
    =0 => eq. (39)
%%%%%%%%%%%%%%%%%%%%%%%%%%%%%%%%%%%%%%%%%%%%%%%%%%%%%%%%%%%%%%%%%%%%%%%%
%Script 4d: input is integrFxy2 and output is (41-48)
%%%%%%%%%%%%%%%%%%%%%%%%%%%%%%%%%%%%%%%%%%%%%%%%%%%%%%%%%%%%%%%%%%%%%%%%
Em0=IntFxy2b(trms == epson^3);
Em0a=expand(subs(Em0,{du00xyiJ},{0})); % Aplication of eq. (19) to Em0
Em0v11=expand(subs(Em0a,{dv10xykm,dv10xyij,dv10xykM,dv10xyiJ,dv10xycm,dv10xyck,
    dv10xycM,dv10xycK},...
        {0,0,0,0,0,0,0,0})); %v10=0 => eq. (41)
Em0v10=expand(subs(Em0a,{dv11xykM,dv11xyiJ,dv11xykm,dv11xyij,dv11xycM,dv11xycK,
    dv11xycm,dv11xyck},...
        {0,0,0,0,0,0,0,0})); %v11=0 => eq. (46)
```

Appendix D

Extension to the *homogenize* function

The following code lines enable the visualization of the deformed configuration of the unit cell, resulting from each of the three characteristic displacements.

```
%%%%%%%%%%%%%%%%%%%%%%%%%%%%%%%%%%%%%%%%%%%%%%%%%%%%%%%%%%%%%%%%%%%%%%%%%%%%
%Plot initial mesh + final mesh resulting from the displacements fields
%%%%%%%%%%%%%%%%%%%%%%%%%%%%%%%%%%%%%%%%%%%%%%%%%%%%%%%%%%%%%%%%%%%%%%%%%%%%
%Coordinates of the nodes of the undeformed shape
cc=zeros(2*(nelx+1)*(nely+1),1); %vector containing the coordinates (first
px=0:dx:lx;                      %x, then y of each node, respecting the
py=ly:-dy:0;                     %node numeration without periodic bcs
kk=1;
for aa=1:2*(nely+1):2*(nelx+1)*(nely+1)-1
    for bb=aa:2:aa+2*(nely+1)-1
    cc(bb)=px(kk);
    end
    kk=kk+1;
end
hh=1;
for aa=2:2*(nely+1):2*(nelx+1)*(nely+1)
    for bb=aa:2:aa+2*(nely+1)-2
    cc(bb)=py(hh);
    hh=hh+1;
    end
    hh=1;
end
% Recover characteristic displacements for full mesh
chis1=reshape(chi(:,1),2*nely,nelx); chis2=reshape(chi(:,2),2*nely,nelx);
chis3=reshape(chi(:,3),2*nely,nelx); chis1(end+1,:)=chis1(1,:);
chis1(end+1,:)=chis1(2,:); chis1(:,end+1)=chis1(:,1);
chis2(end+1,:)=chis2(1,:); chis2(end+1,:)=chis2(2,:);
chis2(:,end+1)=chis2(:,1); chis3(end+1,:)=chis3(1,:);
chis3(end+1,:)=chis3(2,:); chis3(:,end+1)=chis3(:,1);
chi_n1=(0.1/max(chis1(:)))*chis1(:); chi_n2=(0.1/max(chis2(:)))*chis2(:);
chi_n12=(0.1/max(chis3(:)))*chis3(:);
%Coordinates of the nodes of the deformed shape
cc_d1=cc+chi_n1; cc_d2=cc+chi_n2; cc_d12=cc+chi_n12; %From X11, X22, X12
%Plot undeformed vs. deformed shapes
ccn=[cc_d1 cc_d2 cc_d12];
%Plot undeformed vs. deformed shapes
%X11
fk=2;
for gl=1:3
figure(fk)
   for ii=0:dy:ly
       plot(0:dx:lx,ii,'ro', 'MarkerSize', 5,'linewidth',2.5,'Color',...
           [0 0 0.5]); hold on;
       plot([0 lx],[ii ii], ':', 'MarkerSize', 5,'linewidth',1.5,...
           'Color',[0 0 0.5]);hold on;
       for jj=0:dx:lx
       plot([jj jj],[0 ly], ':', 'MarkerSize', 5,'linewidth',1.5,...
           'Color',[0 0 0.5]);hold on;
```

```
        end
    end
    hold on;
    plot(ccn(1:2:2*(nelx+1)*(nely+1)-1,gl),ccn(2:2:2*(nelx+1)*(nely+1),gl),...
        'ro', 'MarkerSize', 5,'linewidth',2.5,'Color',[0 0.5 0]);
    hold on;
    ii=1;
    for aa=1:2*(nely+1):2*(nelx+1)*(nely+1)
        bb=aa+2*(nely+1)-2;
        if ii~=bb
        plot([ccn(aa:2:bb-2,gl) ccn(aa+2:2:bb,gl)],...
        [ccn(aa+1:2:bb-1,gl) ccn(aa+3:2:bb+1,gl)],...
        '-', 'MarkerSize', 5,'linewidth',2,'Color',[0 0.5 0]);hold on;
        end
        ii=ii+1;
        hold on;
    end
    hold on;
    for ll=1:2:2*nely-1
        plot([ccn(ll:2*(nely+1):ll+2*(nely+1)*nelx,gl) ...
            ccn(ll+2:2*(nely+1):ll+2*(nely+1)*nelx+2,gl)],...
        [ccn(ll+1:2*(nely+1):ll+2*(nely+1)*nelx+1,gl) ...
        ccn(ll+3:2*(nely+1):ll+2*(nely+1)*nelx+3,gl)],...
        '-', 'MarkerSize', 5,'linewidth',2,'Color',[0 0.5 0]);hold on;
    end
    title('blue = undeformed shape, green = deformed shape');
    fk=fk+1;
end
```